2019

On the Fuel Spray Applications of Multi-Phase Eulerian CFD Techniques

Gabriel Lev Jacobsohn
University of Massachusetts Amherst

ON THE FUEL SPRAY APPLICATIONS OF MULTI-PHASE EULERIAN CFD TECHNIQUES

A Thesis Presented

by

GABRIEL L. JACOBSOHN

Submitted to the Graduate School of the
University of Massachusetts Amherst in partial fulfillment
of the requirements for the degree of

MASTER OF SCIENCE IN MECHANICAL ENGINEERING

September 2019

Mechanical and Industrial Engineering

ON THE FUEL SPRAY APPLICATIONS OF MULTI-PHASE EULERIAN CFD TECHNIQUES

A Thesis Presented

by

GABRIEL L. JACOBSOHN

Approved as to style and content by:

David P. Schmidt, Chair

J. Blair Perot, Member

Juan M. Jiménez, Member

Sundar Krishnamurty, Department Chair
Mechanical and Industrial Engineering

DEDICATION

To the magic rocks that did all the math.

ACKNOWLEDGMENTS

First and foremost, I'd like to thank my family, whose support was crucial in getting me to the finish line. Thanks also to my advisor, Professor Schmidt, whose guidance, trust, and advocacy made for a great graduate school experience and helped me grow both as a student and as a person. I'd also like to thank my committe members, Professors Perot and Jiménez, for being helpful and flexible throughout this process. I'd also like to thank Professor Perot for challenging me to be a better student in each of the whopping four classes I took with him throughout my time at UMass. Next, the mentorship and opportunities I received from Ronald Grover Jr. at General Motors were invaluable as I began my foray into sprays and industry research in general. Completing this work punctually would have been extremely difficult without the access to dedicated computing resources at Argonne National Laboratory generously granted by Dr. Christopher Powell, who also provided experimental data from Argonne throughout my studies. Dr. Brandon Sforzo at Argonne also has my thanks for providing me with Beta access to the X-Ray scanned geometries which I used for much of this thesis. I am also grateful for Dr. Daniel Duke's advice, as well as for his willingness to share detailed experimental data at a moment's notice. Next, I'd like to thank the my many labmates both past and present (Peetak, Chinmoy, Hannah, Brandon, Alden, Michael, Mateus, Paul, Volodymyr, Sampath, Piotr, Jen, and Catherine) for their help and comraderie throughout my time here. I will always remember the laughs and good times we've shared, and am lucky to have worked in such a fun environment with so many good people. Finally, I'd like to thank Dr. Eli Baldwin, whose mentorship from my first day in the lab as an undergrad, through a summer of consulting work, to job hunting and beyond has made an enormous impact

on my career. I'd also like to thank you, the reader (if you're out there), for perusing the result of two years worth of hard work, late nights, and spent CPU cycles.

ABSTRACT

ON THE FUEL SPRAY APPLICATIONS OF MULTI-PHASE EULERIAN CFD TECHNIQUES

SEPTEMBER 2019

GABRIEL L. JACOBSOHN

B.S, UNIVERSITY OF MASSACHUSETTS, AMHERST

M.S, UNIVERSITY OF MASSACHUSETTS, AMHERST

Directed by: Professor David P. Schmidt

Eulerian-Eulerian Computational Fluid Dynamics (CFD) techniques continue to show promise for characterizing the internal flow and near-field spray for various fuel injection systems. These regions are difficult to observe experimentally, and simulations of such regions are limited by computational expense or reliance on empiricism using other methods. The physics governing spray atomization are first introduced. Impinging jet sprays and Gasoline Direct Injection (GDI) are selected as applications, and modern computational/experimental approaches to their study are reviewed. Two in-house CFD solvers are described and subsequently applied in several case studies. Accurate prediction of the liquid distribution in a like-doublet impinging jet spray is demonstrated via validation against X-Ray data. Turbulence modeling approaches are compared for GDI simulations with dynamic mesh motion, with results validated against previously available experimental data. A new model

for turbulent mixing is discussed. Code performance is thoroughly tested, with new mesh motion techniques suggested to improve scaling. Finally, a new workflow is developed for incorporating X-Ray scanned geometries into moving-needle GDI simulations, with full-duration injection events successfully simulated for both sub-cooled and flash-boiling conditions.

TABLE OF CONTENTS

Page

ACKNOWLEDGMENTS . . . . . **iv**

ABSTRACT . . . . . **vi**

LIST OF TABLES . . . . . **x**

LIST OF FIGURES . . . . . **xi**

CHAPTER

1. INTRODUCTION **1**

2. BACKGROUND **3**

2.1 Spray Physics and Breakup Regimes 3
2.2 Multi-Phase Nozzle Flow 7

2.2.1 Cavitation 7
2.2.2 Flash-Boiling 10

2.3 Experimental Techniques 11
2.4 Computational Fluid Dynamics 13

3. APPLICATIONS **16**

3.1 Impinging Jet Sprays 16
3.2 Gasoline Direct Injection 21

3.2.1 Overview 21
3.2.2 Spray G Target Condition 22
3.2.3 Perennial Challenges 24
3.2.4 CFD Studies 27

4. MODELING APPROACH **31**

4.1 CoSigmaY 31
4.2 HRMFoam 34

5. PRELIMINARY CASE STUDIES **38**

5.1 Impinging Jet Sprays 38
5.2 Gasoline Direct Injection: RANS/LES Comparison 43

5.2.1 Overview 43
5.2.2 Results: Grid Sensitivity Study 47
5.2.3 Results: Moving Needle Simulations 50

5.3 Diffusion Flux Closure Effects 55

6. MOVING MESH SIMULATION WORKFLOW **59**

6.1 Motivation 59
6.2 Geometry Preparation and Case Setup 62
6.3 Results 69

7. SUMMARY **77**

BIBLIOGRAPHY **79**

LIST OF TABLES

Table **Page**

3.1 Spray G target condition and selected parametric sub-conditions. 24

5.1 Operating condition summary. 44

5.2 Summary of mesh sizing statistics. 45

5.3 Time-averaged fuel mass fraction contours for the RANS (left) and LES (right) static cases, $1x$ (upper) and $4x$ (lower) resolutions. 49

6.1 Benchmark test results. 62

6.2 Summary of key nozzle dimensions (all units in microns). 63

6.3 Operating condition summary. 68

LIST OF FIGURES

Figure **Page**

2.1 Spray regime examples, reproduced from Reitz and Bracco [84]. 5

2.2 Example spray regime map, reproduced from Reitz [85]. 6

2.3 Visualition of nozzle flow regimes from laminar (a) to turbulent/cavitating (b,c), to supercavitating/hydraulically flipped (d). 8

2.4 Effects of inlet corner radius on cavitation, adapted from Chaves and Ludwig [23]. 9

2.5 Visualization of flash-boiling regimes, reproduced from [117]. 11

2.6 Example 7BM beamline radiography setup, reproduced from [50]. 13

3.1 F1 engine injector schematic, reproduced from [72]. 17

3.2 Mesh sensitivity in VOF impinging jet simulations, reproduced from [24]. 20

3.3 Comparison of SIDI engine injection strategies with typical homogeneous charge MFI or port fuel injection (PFI). 22

3.4 External visualization of the Spray G geometry showing standardized hole numbering. 23

3.5 Annotated internal Spray G geometry, reproduced from [33]. 23

3.6 Visualization of spray collapse, reproduced from [74]. 25

3.7 Inclusion type defect observed in Spray G nozzle surface, reproduced from [33]. 27

3.8 Surface finish of fs pulse laser drilled nozzle showing periodic surface features, adapted from [88]. 28

3.9 Comparison of EDM (Inj #8) and laser drilled (Inj #4) nozzle sprays at various crank angles, reproduced from [120]. 28

3.10 Simulation of Spray G showing asymmetric cavitation due to inconsistent inlet corner radii, reproduced from [107]. 29

3.11 Total pressure isosurface showing string flash boiling vortices in a Spray G2 simulation, reproduced from [10]. 30

5.1 Visual light image of the impinging jet spray used in the experiments, reproduced from [50]. $Re = 10,300$ 39

5.2 Grid dependence study results based on a sample plane $0.59mm$ downstream of the impingement point. 40

5.3 Example impinging jet spray mesh showing areas of local refinement. 41

5.4 EPL vs. Horizontal position at various downstream displacements, $30ft/s$. The origin is calibrated to the jet crossing point. 41

5.5 EPL vs. Horizontal position at various downstream displacements, $60ft/s$. 42

5.6 EPL vs. Horizontal position at various downstream displacements, $90ft/s$. 42

5.7 Sample of the "$4x$" resolution static needle mesh. 45

5.8 Sample of the LES moving needle mesh. 46

5.9 Detail view of the LES dynamic mesh. Three refinement levels are visible, and the extremely thin boundary layer cells on the nozzle walls are discernable. 46

5.10 Static RANS mass flux results. 47

5.11 Static LES mass flux results. 48

5.12 Pope criterion results, "$4x$" resolution LES case. $kRatio$ represents the fraction of the total (SGS and resolved) kinetic energy generated by the SGS model. 50

5.13 Comparison between the simulated and experimentally measured ROI for the moving needle simulations. 51

5.14 Projected mass comparison at $t = 407\mu s$. 52

5.15 Density sample plane comparison at $t = 407\mu s$, $z = 2mm$. 53

5.16 RANS turbulent vortices, $t = 407\mu s$. 54

5.17 LES turbulent vortices, $t = 407\mu s$. 55

5.18 Average projected mass profiles for the Fick's law and Demoulin et al. diffusion flux closures. 57

5.19 Cut plane of the instantaneous diffusion flux (Demoulin et al. flux closure) in the NCG mass fraction transport equation during quasi-steady state. 58

6.1 Benchmark test results. 61

6.2 Visualization of the experimental and nominal geometries before and after stitching. 64

6.3 Sample view of the Star-CCM+ mesh for the Spray G 28 injector at 10 microns of needle lift. 65

6.4 Outside view of a sample SnappyHexMesh grid, showing accurate capture of intricate surface features. 66

6.5 Detail view of a sample SnappyHexMesh grid near a nozzle to counterbore step, showing local refinement to capture the sharp region. 67

6.6 Downstream mesh refinement for the SnappyHexMesh grids. 68

6.7 Initial fuel mass fraction conditions. 69

6.8 Initial vapor volume fraction conditions, ANL-G2 conditions. 70

6.9 Comparison of the simulated and experimentally observed projected mass. Results are time-averaged over the quasi-steady portion of injection. 71

6.10 Projected mass comparison at $t = 407\mu s$. 72

6.11 Time-averaged density contour comparison at z=2mm downstream of the injector tip. 74

6.12 Visualization of vortices in the sac during the ANL-G simulation. 75

6.13 End of injection results, ANL-G condition. Fuel mass fraction (left) and density contours (right). 76

6.14 End of injection results, ANL-G2 condition. Fuel mass fraction (left) and density contours (right). 76

CHAPTER 1

INTRODUCTION

The world's demand for energy continues to increase, with global energy usage rising by a total of 2.1% in 2017 alone [5]. Oil continues to serve as the primary source of energy for this global demand, and is forecast to continue dominating through 2040 based on current economic and political forecasts [4]. These factors have combined to create a forecasted 50% incease in global greenhouse gas emissions by 2050, increasing the already serious concerns about climate change [3]. The transportation sector is forecast to remain the largest end-use source of carbon dioxide emissions for the forseeable future[6]. The aerospace industry in particular is still wholly reliant on fossil fuels, as the energy densitites typical of modern batteries are still too low to support air travel. The battery pack to match the heat content of the fuel in a typical Airbus A320, for example, would exceed the aircraft's maximum takeoff weight on its own [54]. Electric vehicles, while largely improved in recent years, remain too expensive for widespread adoption [103].

Given the transportation sector's continued reliance on liquid fuels, research into fuel injection technology is critical. Controlling the mixture distribution inside a combustion chamber is key to achieving clean, efficient combustion, rendering thorough understanding and control of the spray from a fuel injector critical. Hardware based testing of fuel sprays is expensive and cumbersome, especially under combustion relevant conditions. Simulations of fuel sprays using Computational Fluid Dynamics (CFD) are a promising alternative, but require additional development. In particular, modeling the spray near the injector, as well as the flow inside the injector itself,

remains challenging. The present work seeks to improve upon a promising solution to these modeling challenges.

CHAPTER 2

BACKGROUND

2.1 Spray Physics and Breakup Regimes

Literature on a quantitative understanding of liquid jet atomization physics may be traced as far back as 1873, when Plateau noticed that jets became unstable and broke into smaller ligaments when their lengths exceeded their diameters by a factor of π [77]. He argued that under quasi-static conditions, surface tension would then draw each ligament into a spherical droplet which has a smaller surface area than a cylinder for a given fluid volume. Surface tension carries the dimensions of energy per unit area, so a spherical droplet is therefore a lower energy state for the fluid than a cylinder once past the instability point. Rayleigh expanded on this explanation in 1879 by describing some inertial effects of the breakup mechanism, using stability analysis to reveal that disturbances with wavelengths larger than the jet's circumference were amplified until the ligaments could pinch off [81, 82]. He also noted that disturbances with wavelengths roughly 9 times the jet radius grew much faster than others, resulting in an ability to predict the most common drop size and breakup time. These two findings encompass the Plateau-Rayleigh instability, which drives what is generally known as Rayleigh mode breakup.

Other perennial works expanded upon and generalized this early theory. Weber revealed that air resistance and viscosity both play important roles in jet breakup speed [115]. Taylor then used potential flow theory to characterize the behavior of a fluid being accelerated within another, arguing that the density ratio between the fluids governs the growth of instabilities on the interface [110]. This formed the basis

for what is now commonly known as Taylor mode breakup (often referred to as simply atomization), wherein a fluid injected into another is broken apart into droplets much smaller than the initial jet diameter if it carries sufficient inertia. These works suggest that understanding the competition between inertia, viscosity, and surface tension is crucial to predicting the behavior of a spray. The Reynolds, Weber, and Ohnesorge numbers, respectively given by equations (2.1), (2.2), and (2.3), offer a convenient way to quantify which effects are dominating.

$$Re = \frac{\rho v D}{\mu} \tag{2.1}$$

$$We = \frac{\rho v^2 D}{\sigma} \tag{2.2}$$

$$Oh = \frac{\mu}{\sqrt{\rho \sigma D}} \tag{2.3}$$

In the Reynolds number, ρ is the fluid density, v is the velocity, and D is the hydraulic diameter, which is usually the orifice diameter in atomization studies. This number may be interpreted as a measure of whether advection or viscous diffusion is the dominant process in the flow, and is of course a dimensionless measure of momentum. The Weber number provides a ratio of the fluid's inertia and its surface tension, σ. For atomization cases, ρ is usually the density of the ambient gas, v is the relative velocity, and D is the characteristic length scale (usually the droplet diameter). The Ohnesorge number compares the effects of viscosity and surface tension, with the orifice diameter usually used for the characteristic length. The lack of an inertial dependence in the Ohnesorge number renders it a useful constant when describing a particular spray system. These three parameters allow for the demarcation of jet breakup regimes, in which different dominant spray characteristics are observed as We and Re increase for a given Oh.

Four spray regimes are generally agreed upon today, though their boundaries are still debated. These regimes are summarized below according to the thorough characterization by Reitz [85], with examples presented in figure 2.1.

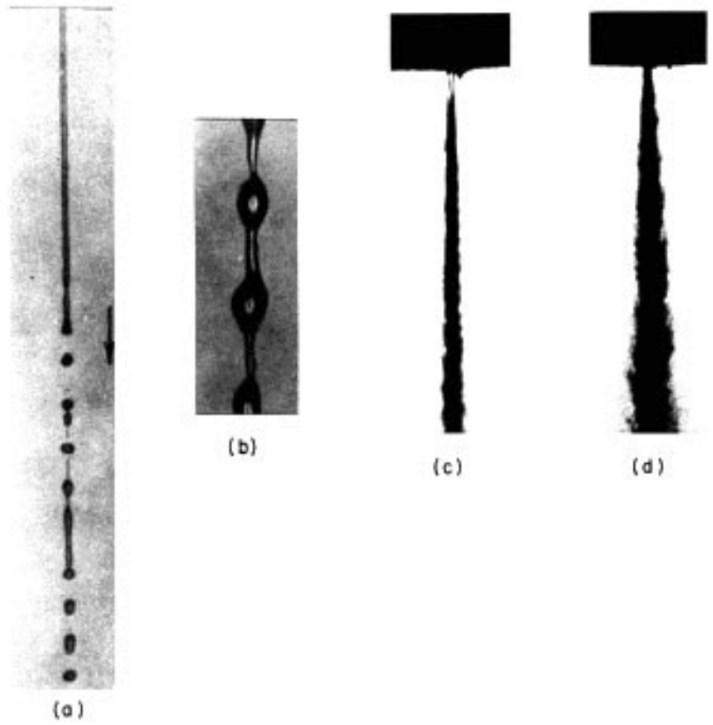

Figure 2.1: Spray regime examples, reproduced from Reitz and Bracco [84].

1. Rayleigh breakup (Figure 2.1a): The the Plateau-Rayleigh instability produces droplets of roughly similar diameter to the jet.

2. First-Wind induced breakup (Figure 2.1b): Aerodynamic effects exacerbate the growth of unstable waves on the interface, producing droplets with similar diameter to those of Rayleigh breakup.

3. Second-Wind induced breakup (Figure 2.1c): Aerodynamic effects are much more violent, leading to the growth of shorter wavelength disturbances. Droplet sizes are reduced, and the liquid core near the nozzle exit is shortened.

4. Atomization (Figure 2.1d): No visible liquid core exists, and droplet sizes are further decreased. The dominant breakup mechanisms are still being studied.

An example breakup regime map is provided by figure 2.2. It is clear that, for a given Ohnesorge number, the spray's regime is determined solely by its Reynolds number. As the Reynolds number increases through the regimes, aerodynamic effects due to the relative velocity between the liquid and gas dominate surface tension to an ever larger degree. This dominance is especially clear in the atomization regime, where the lack of a visibly intact liquid jet at the orifice exit suggests that surface tension has been completely overcome and the growth of unstable waves on the interface no longer governs the breakup rate. This will form the basis of a key modeling assumption, wherein the details of the liquid-gas interface are neglected altogether.

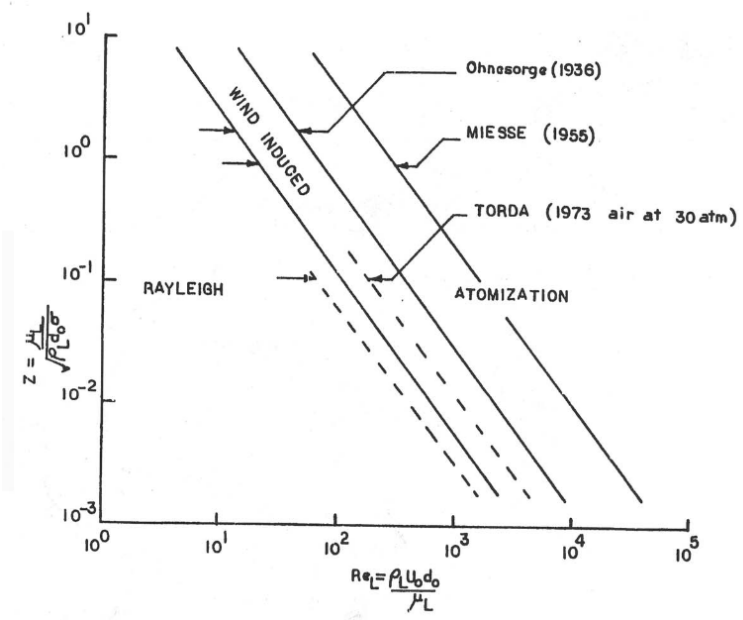

Figure 2.2: Example spray regime map, reproduced from Reitz [85]. The horizontal axis displays the liquid Reynolds number, while the vertical axis denotes the Ohnesorge number, often referred to as Z.

2.2 Multi-Phase Nozzle Flow

2.2.1 Cavitation

The local low-pressure regions generated by a separating flow often fall below the liquid's saturation pressure, resulting in the rapid phase change known as cavitation. This phenomenon often occurs at the inlet of straight, round pipes. The cavity formed downstream of the inlet, often referred to as the vena contracta, reduces the cross-sectional area available for liquid flow. The discharge coefficient C_d, shown in equation (2.4), provides a quantitative measure of the losses due to such restrictions, and is a standard measure of nozzle efficiency. Here, $\dot{m}$ is the liquid mass flow, A is the physical cross-sectional area of the nozzle, ρ is the liquid density, and P_u and P_b respectively represent the pressures upstream and downstream of the nozzle. This compares the actual mass flow rate through the nozzle to the ideal flow rate based on the Bernoulli velocity. The discharge coefficient may be broken into separate velocity and area coefficients to represent different sources of losses, but the total C_d provides more useful information in this case.

$$C_d = \frac{\dot{m}}{A\sqrt{2\rho(P_U - P_B)}} \tag{2.4}$$

The reduction in a straight nozzle's discharge coefficient due to phase change is easily predicted using Nurick's classic cavitation model [70], which is introduced in equation (2.5). The model compares the local pressure conditions to the prevailing vapor pressure, P_v. This comparison is then used to adjust the contraction coefficient C_c, which is described in equation (2.6) according to Hall's experimental results [40]. It is clear that C_c quickly approaches the limit of 0.62 as the upstream area increases. Assuming that this limit has been reached is a safe assumption in most practical cases. This model accurately captures the progressive constriction of the flow as the pressure differential across the nozzle increases relative to the fluid's vapor pressure [98].

$$C_d = C_c(\frac{P_u - P_v}{P_u - P_b})^{\frac{1}{2}} \tag{2.5}$$

$$C_c = 0.62 + 0.38(\frac{A_{nozzle}}{A_{upstream}})^3 \tag{2.6}$$

As cavitation production increases, the vena contracta expands and the reattachment point of liquid to the wall is pushed downstream. In severe cases, the vapor will persist all the way through the nozzle, often called super-cavitation. The recirculation zone present within the vena contracta is then exposed to the atmoshphere downstream of the nozzle, allowing for its entrainment upstream. If the downstream gas propagates to the nozzle's inlet corner, cavitation ceases completely. This phenomenon, known as hydraulic flip, produces a visibly smooth jet. The turbulence generated by the flow's separation and/or cavitation is eliminated, thereby inhibiting atomization outside the nozzle. However, if the flip is only partial and gas is entrained but does not reach the inlet corner, turbulence is still generated and atomization is not adversely affected [104]. Figure 2.3 provides examples of these flow regimes.

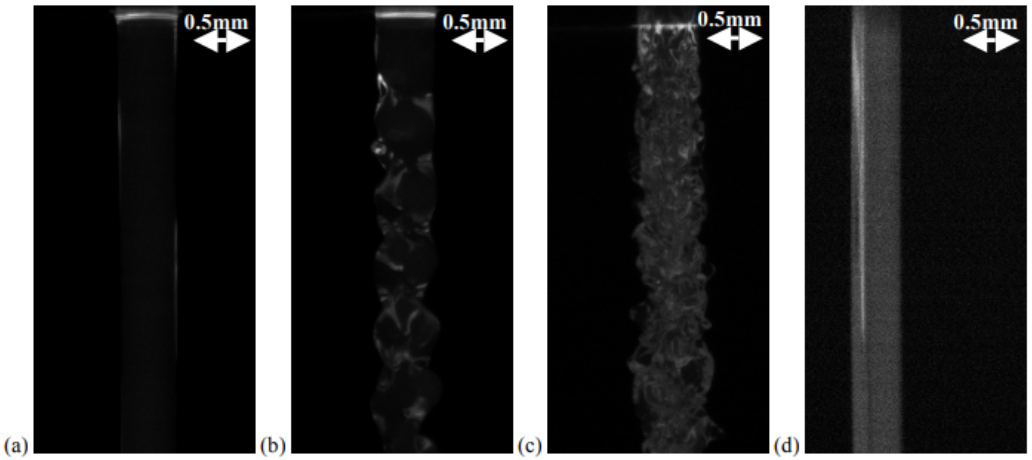

Figure 2.3: Visualition of nozzle flow regimes from laminar (a) to turbulent/cavitating (b,c), to supercavitating/hydraulically flipped (d). Reproduced from [22].

Finally, it is crucial to consider the effects of the geometry of the inlet on the production of cavitation. Nurick's model, for example, is only valid for straight nozzles

with a sharp inlet corner. As the inlet corner becomes rounded, flow separation is reduced and the low pressure region responsible for cavitation is diminished. This transition happens quickly, with cavitation fully eliminated when the inlet corner radius is 14% of the nozzle diameter [70]. The rapid transition from cavitating to single-phase flow is demonstrated in figure 2.4.

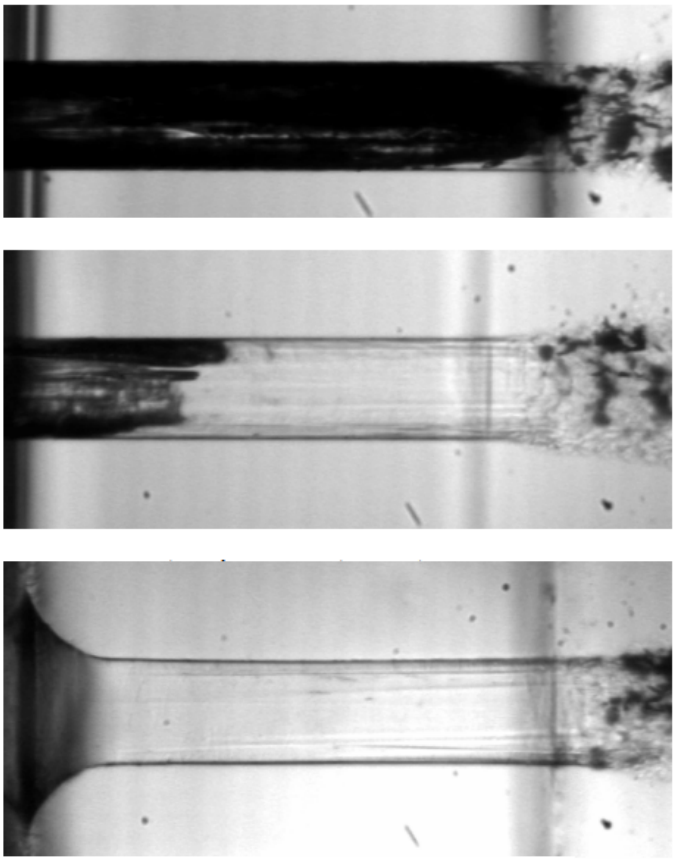

Figure 2.4: Effects of inlet corner radius on cavitation, adapted from Chaves and Ludwig [23]. From top to bottom: Sharp, $30\mu m$ radius, and $170\mu m$ radius inlet corners. $207\mu m$ diameter nozzle, Re=22000.

2.2.2 Flash-Boiling

Cavitation is considered an interially driven process, where the timescale of momentum transfer is more important than that of the inter-phase heat transfer. However, as the liquid temperature increases, the mechanism of phase change transitions towards that of typical thermal-driven boiling. A somewhat ambiguous regime exists where a liquid may vaporize due to a decrease in the local static pressure, but the rate of the process is governed by interfacial heat transfer. A flash-boiling spray, where a hot liquid leaving a nozzle vaporizes due to a back pressure below the liquid's saturation pressure, falls into this regime.

The severity of flash-boiling is usually described in terms of the degree of superheat, or a $\frac{P_a}{P_s}$ ratio, where P_a is the ambient pressure outside the nozzle and P_s is the prevailing liquid saturation pressure. The Jakob number, introduced in equation (2.7), may be used to describe the degree of superheat. This number compares the liquid's sensible heat to its enthalpy of vaporization, essentially quantifying the amount of energy available to produce phase change. The liquid's saturation temperature, T_s, decreases with the ambient pressure, so a low $\frac{P_a}{P_s}$ and high Ja both indicate a high degree of superheat.

$$Ja = \frac{C_p(T - T_s)}{h_{fg}} \tag{2.7}$$

Wu et al. suggest three flash-boiling regimes demarcated by $\frac{P_a}{P_s}$, as demonstrated in figure 2.5 [117]. The first is the sub-cooled condition, where $\frac{P_a}{P_s} > 1$ and no vaporization occurs. As $\frac{P_a}{P_s}$ falls below 1 and vaporization begins, phase change is present in the nozzle but a liquid core is still visible. This is the transitional regime. As $\frac{P_a}{P_s}$ decreases, more vaporization will occur in the nozzle and the liquid core will diminish. The flare-flash regime, which begins at a $\frac{P_a}{P_s}$ of 0.3 according to Wu et al., is reached when no liquid core is visible outside the nozzle.

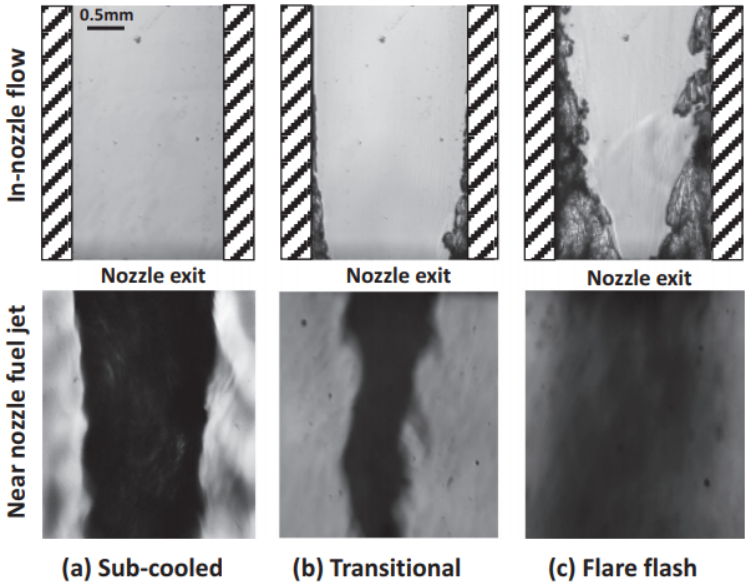

Figure 2.5: Visualization of flash-boiling regimes, reproduced from [117].

2.3 Experimental Techniques

A variety of fuel-spray characteristics are measurable using well-established experimental diagnostic techniques. Measuring the rate of injection (ROI) of a given fuel injector is possible with specialized "long-tube" meters, which function by correlating pressure wave propagation through a chamber to fuel quantity [16]. Common laser or photographic techniques may be used to characterize ambient gas velocities, drop sizes, spray angles, and spray tip penetrations. Determining the density distribution of fuel in a spray is of particular importance for injector development and model validation. Laser-induced fluorescence (LIF), in which the energy emitted by a material excited by a laser is correlated to the material concentration, would seem capable of such measurements. However, the dense, irregular droplets, along with the optical properties of typical fuels, results in significant beam extinction, scattering, and attenuation near the injector exit which can result in accuracy problems [101, 18]. Optical techniques also fail to characterize the internal nozzle geometry and fuel flow patterns for typical metal fuel injectors.

X-Ray techniques have emerged as an attractive alternative, and have been used extensively to visualize and quantitatively analyze flows in recent years. Heindel, in a thorough review of the applications of such techniques, attributes this rise in popularity to the improved performance and attainability of digital detectors and computerized post-processing [42]. In the context of fuel-spray experiments, X-Ray based radiography and tomography are particularly useful. Radiographic density measurements function on the premise that as a focused monochromatic X-Ray beam passes through a material, a portion of it is attenuated. If the attenuation coefficient of the material is measured or known, the reduction in beam intensity can be directly related to the amount of material in the path of the beam using the Beer-Lambert law. A raster scan can then be performed to yield a 2D projection of the density of the material. Tomography measurements are similar, but rely on images of a wide, polychromatic X-Ray beam passing through an object rather than point-wise measurements from a focused, monochromatic beam. Using the polychromatic beam allows more of the metal penetrating high energy photons to be retained, whereas a monochromatic beam makes quantitative attenuation measurements easier to calibrate. If a series of 2D images are captured from a sufficient number of vantage points, tomographic reconstruction allows for the computation of a 3D view of an object that is not directly measurable. This is the same principle used in a standard medical CT (computed tomography) scan.

Time-resolved spray radiography measurements and tomography scans of metal nozzles are also possible, but X-Ray sources with sufficient intensity are not widely available. The 7BM beamline at Argonne National Laboratory (ANL) was designed to provide access to a strong enough source for exactly such purposes [55]. The facility is driven by insertion devices using the 7-GeV synchrotron beam of the Advanced Photon Source at ANL [1]. All of the X-Ray based data referenced in this work were gathered at this beamline. An example radiography setup for the beamline is shown

in figure 2.6. Here, the white beam generated by the insertion device is trimmed by slits, made monochromatic, focused into a narrow beam, and passed through the spray onto the detector. The spray itself is then translated by moving the injector to generate a raster scan. A more thorough description of the beamline is given by Kastengren et al. [55]. Finally, a metal-penetrating tomography setup for the beamline is described by Matusik et al. [60].

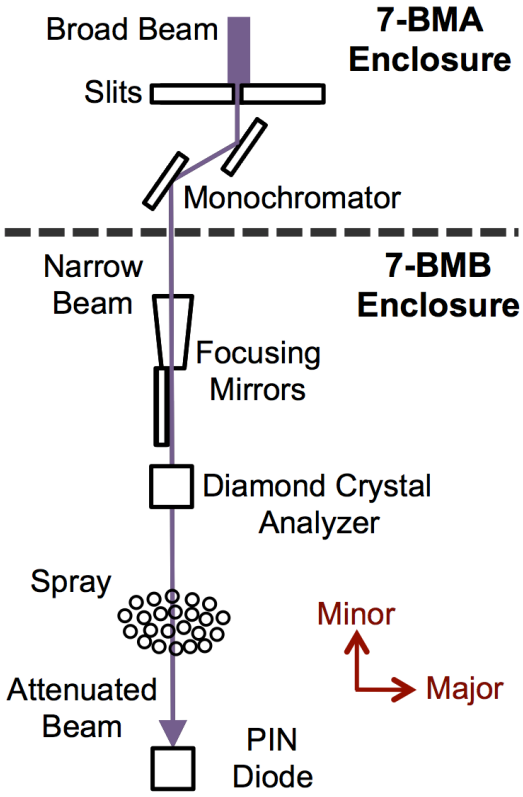

Figure 2.6: Example 7BM beamline radiography setup, reproduced from [50].

2.4 Computational Fluid Dynamics

As the availability and power of high-performance computing (HPC) resources continue to increase, computational fluid dynamics (CFD) modeling of sprays has grown into a widespread industry practice. CFD allows for unique cost savings and increased insight when compared with experimental testing, but considerable effort

is required to develop and validate models capable of simulating new problems. The multi-phase, turbulent, and compressible effects that govern sprays must all be captured, so spray models are particularly complex. The most popular CFD technique for sprays is based on lagrangian particle tracking, in which discrete particles of liquid are injected into a gas and tracked. The liquid, or discrete phase, is modeled from the Lagrangian reference frame, while the continuous gas phase is modeled using typical Eulerian methods. A multitude of droplet dynamic models may be applied to the particles, allowing for rapid characterization of drop sizing, liquid penetration, and gas velocities for a given spray system. Such Eulerian-Lagrangian (EL) models have been available since the early 1980s [35]. Despite their popularity, EL models have inherent limitations due to their underlying assumption that the liquid is comprised of discrete droplets. The dense liquid core that is often present downstream of the injector exit, as well as all details of the flow inside the nozzle itself, do not contain discrete droplets and cannot be simulated. Typically, an injector model is used instead, essentially rolling all details of such areas into a complex boundary condition that can be developed from experiments [97].

An alternative is to simulate the discrete and continuous phases together in the Eulerian reference frame, which allows for direct simulation of the internal flow and near-field spray. However, capturing the interface between the high-density liquid and low-density gas phases is difficult, as it is essentially averaged over the cell in which it falls. A number of well-established interface tracking methods exist to alleviate this problem. The volume of fluid (VOF), initially proposed by Hirt and Nichols, tracks the liquid volume fraction within each cell and searches for discontinuities suggesting the presence of an interface [45]. An interface reconstruction method may then be used to attempt to rebuild the details of the interface. A popular example is the piecewise-linear interface calculation (PLIC) method, in which a flat interface is placed such that the cell is split into two volumes each sized to contain

the entirety of one of the phases [39]. Another approach is to couple the level set method, which allows for easy tracking of curved fronts [100], to the VOF method. VOF level set (VOF-LS) methods are especially useful for spray simulations, as they reduce smoothing problems associated with capturing the curved interfaces of typical round droplets [108]. These sharp interface approaches can produce extremely high-fidelity simulations, as preserving the interfacial details allows for the direct capture of droplet formation and dynamics. However, even small droplets must be discretized by multiple cells, rendering such methods extremely expensive for the high Re and We sprays typical of modern fuel injection systems.

A third option is to model the discrete and continuous phases in the Eulerian reference frame, but allow the interface to remain diffuse. Simply ignoring the details of the interface is a tremendous simplification, but is justifiable under the correct conditions. Siebers asserts that under typical diesel spray conditions, the inter-phase mass, momentum, and energy transport is limited by turbulent mixing, and is not impacted by interfacial effects [102]. This is in line with the description of the atomization regime in section 1.1, in which surface tension is completely dominated by inertial effects under high We conditions. A turbulent mixing model may then be used to close the system, and primary atomization models may be used to recover drop sizing information. The CFD solvers used in this work seek to apply such an approach to modern fuel spray applications, and will be discussed in detail in Chapter 3. A diffuse interface Eulerian-Eulerian internal flow/near-field spray simulation may also be coupled to an EL model for downstream measurements, in what is generally known as an Eulerian-Lagrangian Spray Atomization (ELSA) approach [15].

CHAPTER 3

APPLICATIONS

3.1 Impinging Jet Sprays

When two liquid jets are directed at one another such that they are self-impinging, a flat liquid sheet is produced which is unstable due to the violent disturbances caused by the jet collisions. Doublet impinging jet fuel injectors take advantage of this to produce accurately distributed, rapidly atomizing sprays. The two main configurations are "like-doublets", where two identically sized liquid jets are collided, and "unlike-doublets", where jets of different geometries are collided and mixed. Unlike doublets can be used to mix fuel and oxidizer jets in a single injector at a desired mixture ratio. Self-impinging injectors are particularly well suited to liquid fueled rocket engines, as they are simple and inherently perform well under high flow rate conditions since they use the jets' kinetic energy to drive breakup. The Saturn V's F1 rocket engine, for example, used rings of like-doublet injectors alternating between fuel and oxidizer as seen in figure 3.1. The F1 was also famous for early combustion instability problems, wherein the fluid and combustion dynamics become coupled and cause damaging pressure fluctuations and vibrations [72].

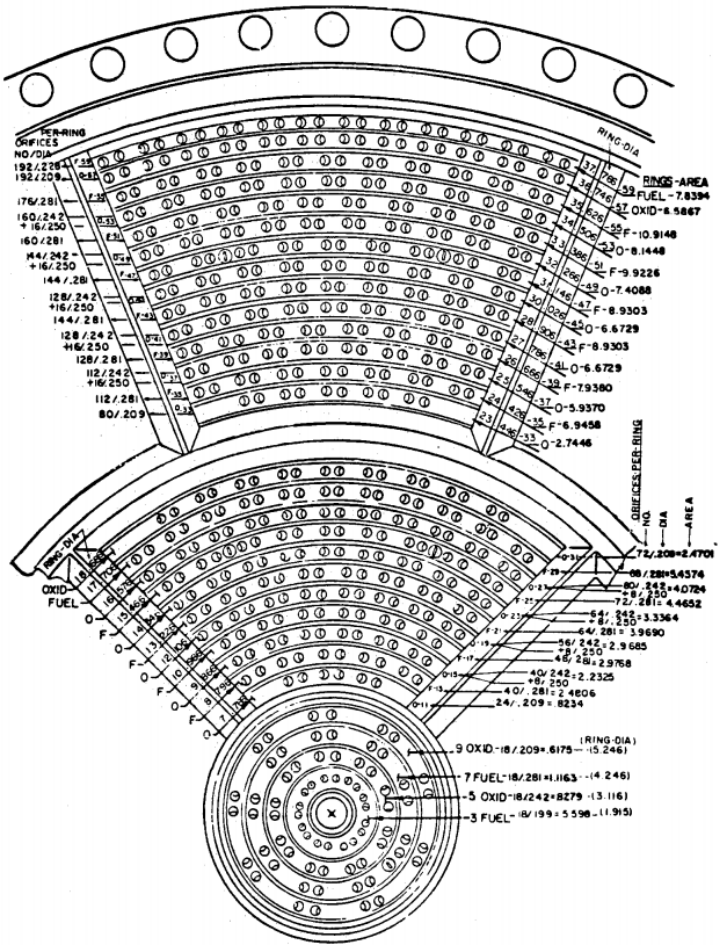

Figure 3.1: F1 engine injector schematic, reproduced from [72].

The F1's instability problems sparked considerable research efforts into self-impinging injectors in the 1950s [72]. Rupe, during thorough experimental parameter studies, observed that the optimal spray distribution from a doublet injector is achieved when the product of the momentum and diameter of the two streams are the same, as is the case in a like-doublet with a single liquid [91, 92]. Dombrowski and Hooper found that for jets with a sufficiently high We, the breakup mechanism is dominated by impact waves rather than aerodynamic instabilities [28]. Hoehn et al., expanding on experiments by Nurick and McHale, investigated various unlike-doublet geometries

and determined that performance near that of circular like-doublet injectors is feasible [46, 71].

More recently, Anderson et al. and Ryan et al. supported Dombrowski and Hooper's findings via phase doppler particle anemometry (PDPA) experiments. They argued that inertial perturbations in the colliding jets are responsible for generating the impact waves, especially in turbulent cases [7, 93]. They also noted that droplet sizes decreased as the jet velocity increased, and that the breakup length of the liquid sheet was heavily dependent on whether the jet was laminar or turbulent. Jung et al. used planar LIF to measure the spray distributions generated by like-doublet injectors [52]. They demonstrated reasonable agreement with a mechanical patternator, attributing the lack of scattering/extinction/attenuation errors to the low thickness of the dense liquid sheet. Their experiments were performed at a single injection pressure of 3 bar, so it is unclear if the reliability of the results would decrease under more practical operating conditions.

Bush and Hasha found that high speed laminar impinging jets formed a symmetric, regular pattern resembling a fishbone [20]. Jung et al. noted that the onset of such a pattern occured at lower jet velocities if slight asymmetries were introduced [53]. Such asymmetries could be caused by slight misalignment between the jets or disturbances in the velocity profiles of either jet, which reinforces the importance of accurately capturing the velocity profile and collision point. Sakisaka et al. performed phase doppler anemometry (PDA) measurements and attempted to predict the liquid sheet location using an analytical model, but did not produce an agreement [95]. Indiana et al. used PDA measurements to verify the trend of decreasing drop sizes with increasing jet velocity, and then correlated their results to mimic industrially relevant reactive sprays. They note that experiments on impinging jet sprays generally do not occur under combustion relevant conditions [48]. Finally, Rodrigues et al. also performed PDPA experiments, arguing that the widely referenced experimental

results of Ryan et al. may be skewed towards larger droplets because of limited dynamic range [87].

While experimental literature on impinging jet sprays was introduced over half a century ago, CFD studies on the topic only began to appear recently. Arienti et al. used a VOF-LS approach coupled to Lagrangian particle tracking to achieve the first viable simulation of a like-doublet spray [9]. Tracking smaller structures from the Lagrangian reference frame allowed them to be removed from the VOF-LS simulation. This, in conjunction with a block-structured adaptive mesh approach, made the computational costs feasible. They simulated the experimental results of Ryan et al., achieving reasonable agreement in terms of pressure fluctuation frequencies and droplet size distributions. However, they noted that grid dependencies could not be ruled out, and that the sheet breakup length was consistently under-predicted.

Chen et al. performed high fidelity VOF simulations, also on the Ryan et al. experiments [24]. Their method used adaptive octree mesh refinement (AMR) to capture the interface without wasting mesh resolution in unimportant areas, and also removed the smallest droplets in the domain to greatly reduce cost. Their results for the droplet size distribution agreed with those of Ryan et al. relatively well, but were shown to be heavily dependent on the maximum refinement level used for the simulations as seen in figure 3.2. Ruan et al. performed a parameter study on a like-doublet spray with $8,000 < Re < 23,000$ and impingement angles from 50 to 110 degrees using an approach similar to that of Chen et al. [90]. They captured various experimental trends qualitatively, but did not account for the increased resolution requirements introduced by increasing Re. Finally, Zhang and Wang investigated the effects of increased/oscillating back pressures, again using a VOF approach with AMR [121]. They note that as the back pressure is increased or oscillates faster, the atomization is enhanced. They also note that the impact wave results in a sinusoidal sheet velocity at the impingement point.

All of these CFD studies took remarkably similar approaches, and as such have similar limitations. None took the effects of compressibility or turbulence into account. The internal flow through the injector was also ignored in all cases, with the jet instead initialized externally with a plug flow, parabolic, or power law velocity profile. More importantly, simulating combustion-relevant conditions is challenging with VOF/VOF-LS methods, as the simulations become progressively more expensive as Re and We increase. In particular, supercritical simulations are not feasible with such approaches. The current work will therefore apply the previously described diffuse interface approach to impinging jet spray simulations.

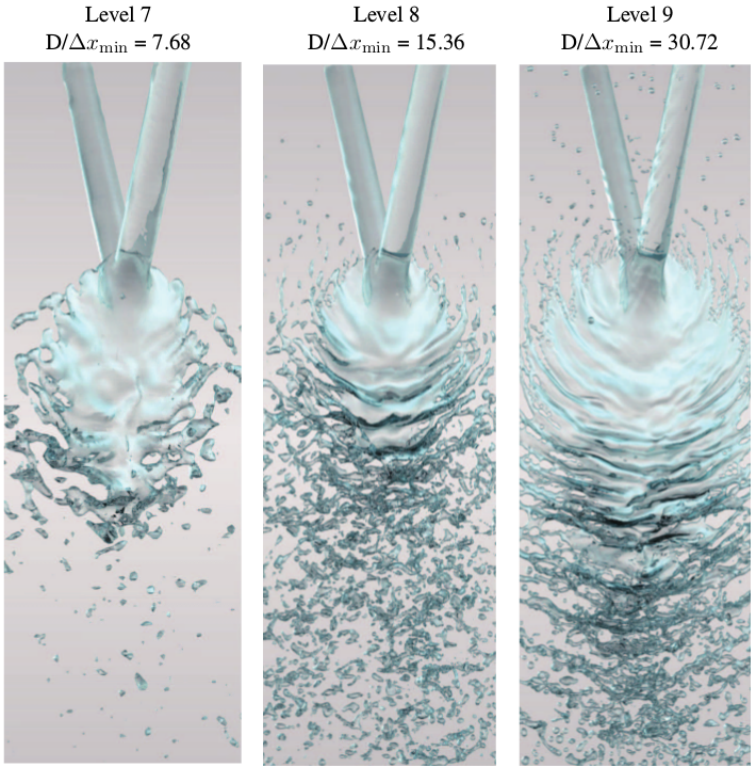

Figure 3.2: Mesh sensitivity in VOF impinging jet simulations, reproduced from [24]. The Reynolds number of the jet was $\approx 12,000$.

3.2 Gasoline Direct Injection

3.2.1 Overview

Economic and regulatory pressures on automotive manufacturers continue to drive efforts aimed at increasing the efficiency and cleanliness of the internal combustion engine. Advances in fuel injection systems remain integral to such efforts, as controlling the temporal/spatial distributions of the fuel-air mixture in the cylinder is key to achieving control over the combustion itself. Traditional fuel injected engines introduce fuel either just downstream of the throttle body (throttle body injection, TBI) or in individual runners on the intake manifold (multi-port fuel injection, MFI), where it is then drawn into the cylinder on the intake stroke of the engine. The latter strategy allows the mixture ratio to be tuned in individual cylinders and reduces the amount of time taken for the fuel to reach the intake valves, thereby offering a greater degree of control compared to TBI at the expense of complexity. A logical extension of this would be to bypass the intake system altogether and introduce fuel directly into the combustion chamber, leading to extremely low-latency control over the amount of fuel in the cylinder. This strategy is commonly referred to as gasoline direct injection (GDI), and is used to create spark ignited direct injected (SIDI) engines.

A unique advantage of GDI over MFI/TBI is that fuel may be injected at any point in the engine cycle. Injecting just before ignition reduces knock at high pressures, which is particularly important for high compression or forced induction applications at full load. The same strategy can be used at partial load by injecting smaller amounts of fuel. This creates a fuel-rich environment near the spark plug to facilitate ignition without having to close the throttle, thereby reducing pumping losses [36]. This is referred to as stratified lean combustion. Stratified combustion strategies require the spray to be directed towards the spark plug. Modern SIDI designs are spray-guided (SG-SIDI), meaning the spray is focused directly towards the plug

without rebounding off of the piston or cylinder wall (see figure 3.3). SG-SIDI engines provide significant fuel economy and emissions performance improvements over older wall guided designs, particularly due to their capability to provide stratified lean combustion over a wide range of operating conditions [31, 73]. However, SG-SIDI engines are also prone to combustion instabilities and flame propagation issues which lead to misfires [75, 76]. Solving these issues requires careful control and understanding of the fuel spray itself.

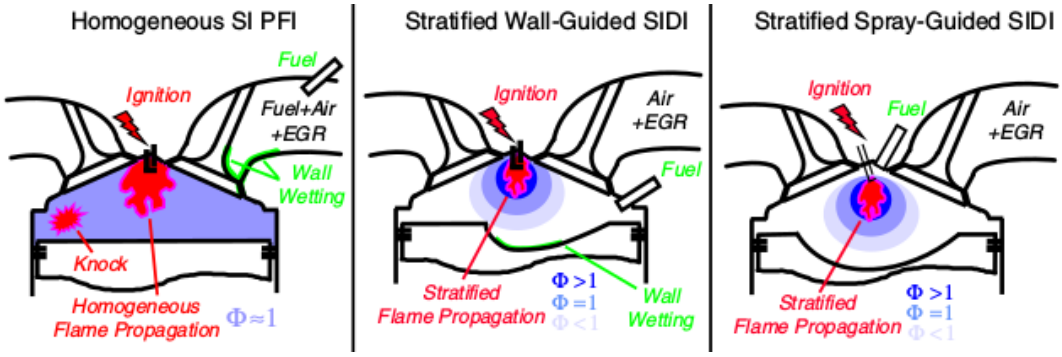

Figure 3.3: Comparison of SIDI engine injection strategies with typical homogeneous charge MFI or port fuel injection (PFI). The mixture ratio relative to stoichiometric conditions is represented by Φ. Adapted from [30].

3.2.2 Spray G Target Condition

Automotive fuel injection systems research represents a complex, multi-disciplinary problem, rendering robust communication and organization between researchers key. Sandia national lab's Engine Combustion Network (ECN) program was introduced to facilitate open and collaborative engine/fuel injection research spanning multiple automakers, parts suppliers, academic institutions, government facilities, and other industry partners in an attempt to solve such challenges [2]. ECN publishes multiple target conditions and standardized research topics, most of which targeted diesel systems until recently. The ECN "Spray G" condition was created specifically to encourage GDI research, as it is largely an extension of diesel research and fit well

with most contributors. Spray G is based on an 8-hole, piezoelectric valve-covered orifice injector produced by Delphi, visualized in Figure 3.4.

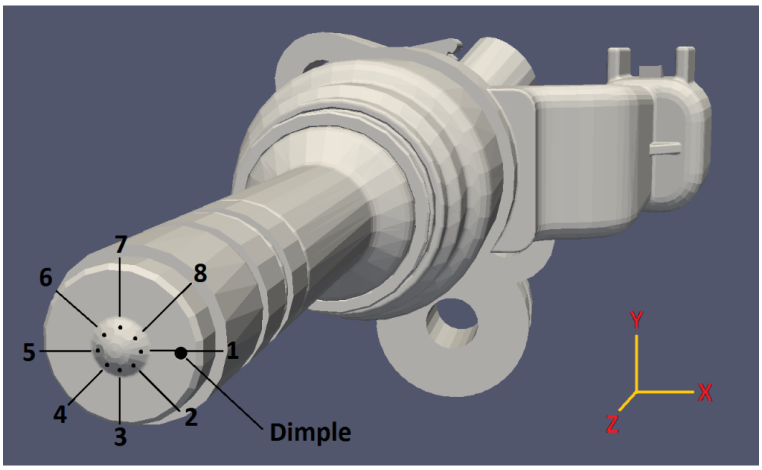

Figure 3.4: External visualization of the Spray G geometry showing standardized hole numbering. Reproduced from the ECN website [2].

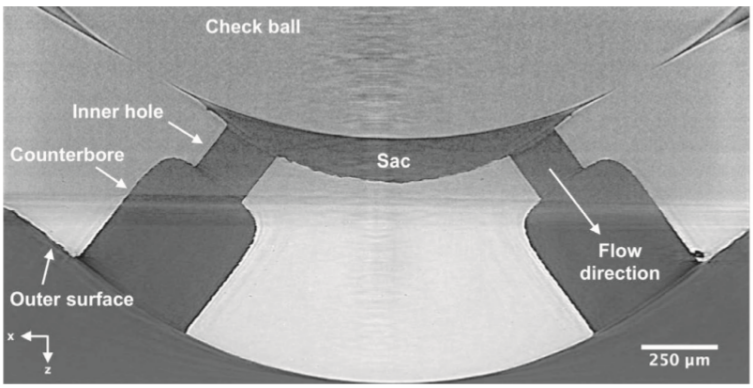

Figure 3.5: Annotated internal Spray G geometry, reproduced from [33].

The internal geometry, shown in Figure 3.5, consists of stepped orifices connected by a "sac" region which serves as an accumulator for high pressure fuel. The check ball, or needle, is raised by the piezoelectric actuator to begin the injection event. Needle lifts for GDI are on the order of $50\mu m$, roughly a quarter of typical diesel lifts [2]. The needle is located by five guides, rendering the flow pattern inherently

assymetric. The target operating conditions, as well as sub-conditions intended to explore a wider portion of the GDI operating envelope, are summarized in table 3.1. Much of the remaining discussion will focus on the Spray G platform.

Table 3.1: Spray G target condition and selected parametric sub-conditions. Table generated based on information from the ECN website [2].

Condition	G	G2	G3	G7	G-M1
Intent	Standard	Flash-Boiling	Early Injection	Strong Collapse	Multiple Injection
Ambient Temp (K)	573	333	333	800	573
Back Pressure (kPa)	600	50	100	2150	600
Duration (ms)	0.680	0.680	0.680	0.680	0.680 Initial 1.0 Dwell/Rest 0.186 Post

3.2.3 Perennial Challenges

Experimental studies have revealed numerous challenges that differentiate GDI research from that of diesel sprays. First, depending on the piston's position during injection, the in-cylinder pressure can fall below the fuel's vapor pressure leading to sustained flash-boiling. To study the effects of such phase change on the injection characteristics, Wu et al. photographed sprays from sub-cooled, transitional, and flash-boiling conditions for a multitude of injector configurations [117]. They found that stronger flash-boiling tended to increase the spray angle, which is in line with earlier research on simpler nozzles by Reitz [83]. Reitz's study also suggests that flash-boiling is generally beneficial for atomization, as fuel droplets decrease in size due to their liquid vaporizing. Zhang et al. performed a photographic study on a single hole injector across a range of degrees of superheat [120]. They observed the same spray angle trend as Wu et al., and also observed that the fuel-gas density ratio was more influencial under sub-cooled conditions. Wu et al. have also shown that flash-boiling conditions cause any liquid fuel present after injection to vaporize

instead of adhering to the tip of the injector, implying the reduction of coking issues related to such tip-wetting [117].

The multi-hole injectors typical of GDI produce multiple tightly spaced fuel plumes. Under certain circumstances, these plumes can interact to the point where they are no longer distinguishable and the spray contains a single large plume. This phenomenon, dubbed spray collapse, serves as another perennial GDI challenge due to its drastic effects on the spray's characteristics (see Figure 3.6). Sphicas et al. shed light on the mechanism of the collapse itself, observing that under normal Spray G conditions, a consistent reverse flow of air was present in the center of the spray between the plumes [106]. This upstream axial entrainment of air, combined with additional air entrainment in the spaces between plumes, established a re-circulating airflow that was sufficient to keep the plumes separated. Sphicas et al. assert that high levels of plume interaction begin to degrade this re-circulation, resulting in a transient reduction in the spray angle as the lack of airflow allows the plumes to move inward. They found that if the plumes continued moving inward, re-circulation was cut off completely and collapse occured.

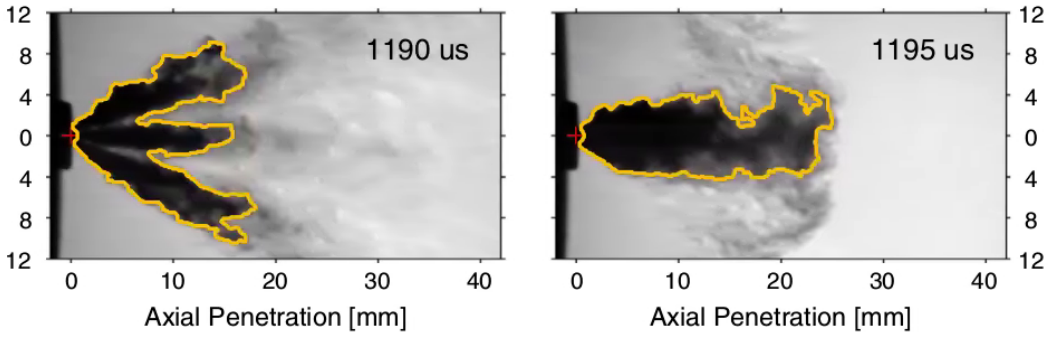

Figure 3.6: Visualization of spray collapse, reproduced from [74].

Payri et al. showed that spray collapse leads to a large reduction in spray angle and an increase in axial penetration [74]. Conservation of momentum links these effects, as the radial momentum of a wide plume is exchanged for axial momentum in a narrow

one. Payri et al. also suggest that high temperature conditions lead to higher rates of fuel evaporation, resulting in an increase in spray angle and consequently higher level of the plume interactions which drive collapse. Finally, they found that higher ambient gas densities increased the likelihood that collapse would occur. Wu et al. also observed partial and total spray collapse in their flash-boiling studies, finding that the axial length of the collapsed region of the spray increased with the degree of superheat [117].

A third challenge is posed by the effects of manufacturing imperfections in the injector on the spray itself. Matusik et al. performed X-Ray radiography and tomography experiments on all eight of the standard Spray G sample injectors to examine the effects of variation between the nozzles. [61]. They observed that the per-hole rate of injection (ROI) varied between the injectors, attributing most of the discrepancy to inconsistencies in the inlet corner radii of the nozzles causing asymmetric cavitation. They also observed higher level changes, including a post-injection fuel dribble, for two of the eight injectors. Duke et al. performed detailed tomography analysis on a single injector, Spray G #28 [33]. They found an average nozzle diameter of approximately $173\mu m$, notably larger than the $165\mu m$ design specification. Significant defects in flow-critical areas were also observed, and the overall surface finish appeared to be rough (see Figure 3.7).

The manufacturing process for the Spray G nozzles is micro-electrical discharge machining (μ-EDM), which is generally considered the industry standard for the microdrilling of fuel inejctors [80]. Slow drilling times [8], in addition to the previously discussed issues of surface roughness, defects, and reproducibility, have led manufacturers to examine possible alternatives to EDM. Laser drilling techniques, previously impractical due to the large heat affected zones and recast layers they create, have become more feasible with the development of ultra-short femtosecond duration pulsed laser strategies [109]. With a sufficiently short laser pulse, the material is ablated

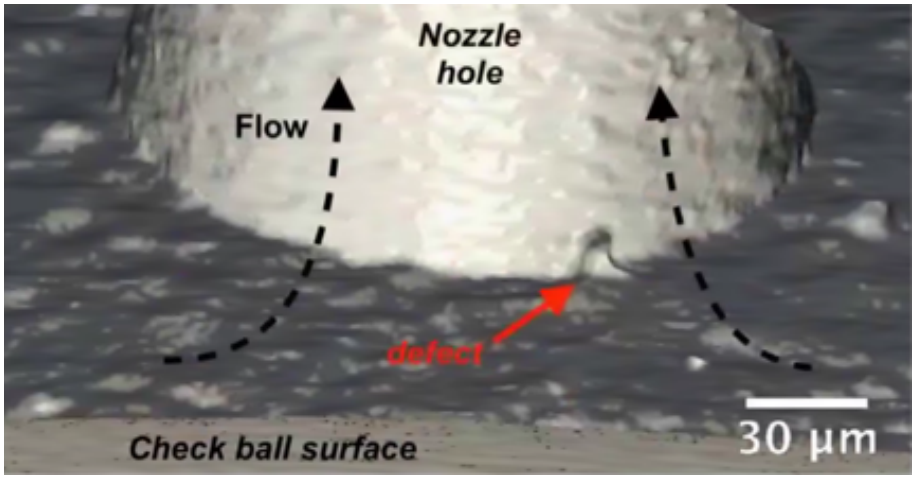

Figure 3.7: Inclusion type defect observed in Spray G nozzle surface, reproduced from [33].

rather than melted away, resulting in much smaller recast layers and heat affected zones [118]. Fuel nozzles manufactured via fs pulsed laser techniques contain sharper, more reproducible features than μ-EDM, but suffer from defects and small cracks due to the rapid material ablation [89, 88]. The surface finish is smoother than that of μ-EDM, and is characterized by the small, uniform ripples visible in Figure 3.8. These differences, while seemingly subtle, can combine to alter the macroscopic characteristics of the spray from a GDI type injector. For example, Zhang et al. compared μ-EDM and laser drilled injectors in an optical engine, observing spray collapse and higher soot emissions for the latter technique under otherwise identical operating conditions as Figure 3.9 demonstrates [120]. Incorporating as-manufactured geometry into CFD simulations of GDI injectors is therefore important.

3.2.4 CFD Studies

CFD simulations have begun to validate/expand upon experimental studies of GDI. Moulai et al. successfully simulated the internal and near-field flow of the Spray G injector using an Eulerian-Eulerian technique, capturing the effects of in-nozzle

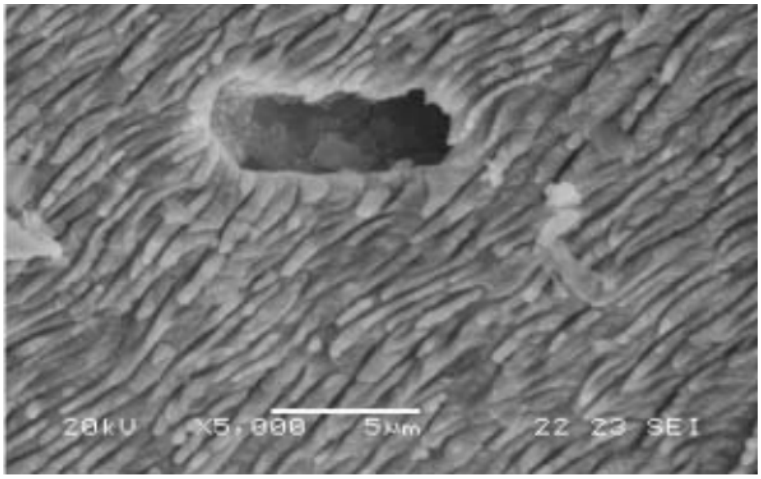

Figure 3.8: Surface finish of fs pulse laser drilled nozzle showing periodic surface features, adapted from [88]. A pit defect is also present.

Figure 3.9: Comparison of EDM (Inj #8) and laser drilled (Inj #4) nozzle sprays at various crank angles, reproduced from [120].

cavitation on the external spray [66]. Strek et al. incorporated the experimentally measured dimensions of the Spray G #28 injector into their simulations [107]. In addition to the per-hole ROI corellating with the hole area, they found that variations in the inlet corner radii produced the asymmetric cavitation visible in Figure 3.10. Baldwin et al. simulated Spray G and G2 injections using mesh motion to capture the effects of needle lift and wobble [10]. In addition to matching the experimentally predicted overall ROI, they observed transient, turbulent hole-to-hole interactions throughout the injection event. These interactions, visualized in Figure 3.11, were comprised of vortices with a vapor core, or string flash boiling. The low needle lifts

typical of GDI, as well as the needle wobble, were thought to encourage generation of the vortices.

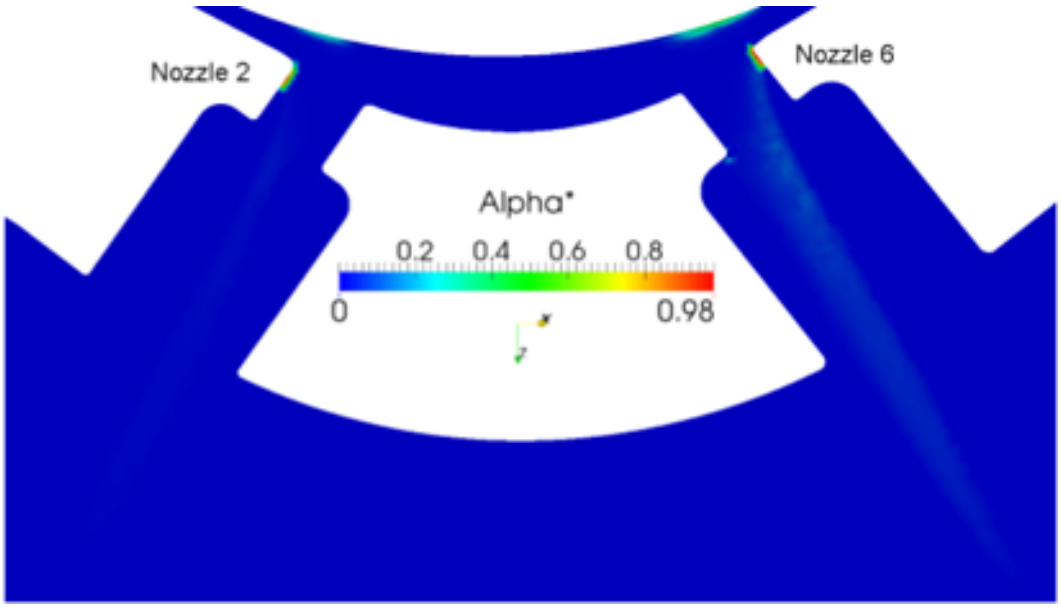

Figure 3.10: Simulation of Spray G showing asymmetric cavitation due to inconsistent inlet corner radii, reproduced from [107]. Alpha represents the fraction of volume occupied by fuel vapor.

Duke et al. combined X-Ray and neutron tomography to create a CFD mesh of the entire Spray G #28 injector, including the upstream sections typically neglected in other simulations, proving that simulating as-manufactured geometry with extremely high fidelity is feasible [32]. Yue et al. used large eddy simulation (LES), transient needle motion, and VOF to simulate a single hole of the as-designed and as-manufactured Spray G #28 injector [119]. The as-manufactured geometry was found to produce a higher number of transient fluctuations in the spray compared to the as-designed nozzle. Mohapatra et al. introduced a needle sealing algorithm, allowing start of injection (SOI) and end of injection (EOI) events to be captured [64]. They verified the vaporization of residual fuel post-injection under flash boiling conditions [65]. Finally, Rachakonda et al. simulated a single-hole nozzle over various levels of

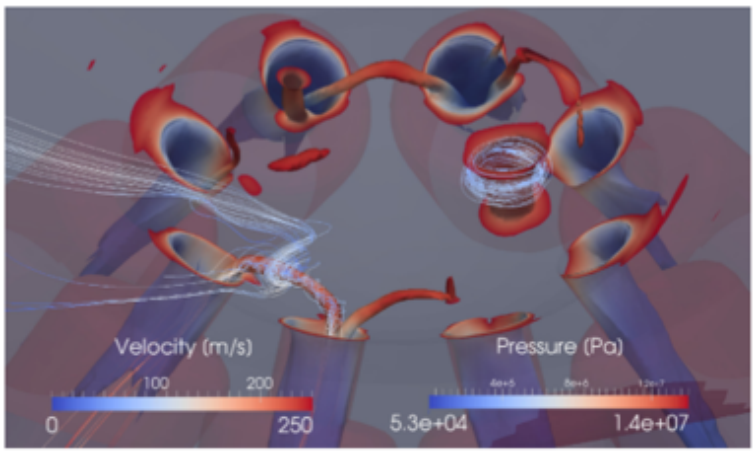

Figure 3.11: Total pressure isosurface showing string flash boiling vortices in a Spray G2 simulation, reproduced from [10].

superheat, finding that wider spray angles occurred under hard-flashing conditions but otherwised remained relatively consistent [79].

CFD simulations of GDI are still limited in number and scope as a whole, especially compared to diesel sprays. A workflow capable of examining transient needle motion, cavitation, flash-boiling, needle opening/closure, and as-manufactured geometry in a single simulation would be a significant expansion of the existing literature, provide richer comparisons with existing experimental data, and allow the effects of various perennial challenges to be weighed against one another. The present work will use a well validated model as a starting point to produce such a workflow.

CHAPTER 4

MODELING APPROACH

The two Eulerian-Eulerian diffuse interface solvers used in this work will now be introduced. The first, CoSigmaY, models liquid injecting into a non-condensable gas (NCG), and accounts for the effects of compressibility and turbulent mixing. The second solver, HRMFoam, adds fuel vapor as a third phase. This necessitates the addition of a phase change model and an accurate thermodynamic property framework. HRMFoam also supports mesh motion, and has recently been expanded with a sealing function to handle needle opening/closure events. Both solvers were developed in-house using the Foam-Extend branch of the OpenFOAM framework [116]. OpenFOAM is popular due to its built-in support for parallelism, polyhedral meshes, RANS/LES turbulence models, and dynamic mesh motion. It also provides a diverse set of pre and post processing utilities, and benefits from a large user base and active community support forums.

4.1 CoSigmaY

CoSigmaY is based on the $\Sigma - Y$ primary atomization model proposed by Vallet and Borghi [114, 19]. The model essentially argues that under the mixing-limited conditions previously described, the small scale details of the interface can be modeled rather than resolved. This is very similar to turbulence modeling, where small velocity fluctuations are modeled via a turbulent viscosity rather than being resolved individually. The model has been used in a variety of solvers to model air blast atomizers [11], pressure-swirl injectors [12], and gas-swirled coaxial injectors [112].

It has also been used extensively in diesel spray modeling, where the high Re and We requirements are easily met [15, 27, 26, 37]. The model has also been validated against DNS for diesel sprays [57].

Vallet and Borghi begin by defining an indicator function, Y, that is unity in liquid regions and zero in gas regions. This allows the mixture to be treated as a single pseudo-fluid if the transport equation for Y, given by equation (4.1), is solved. Over-bars refer to mean, or time averaged, quantities, apostrophes refer to fluctuating quantities, and over-tildes refer to Favre averaged quantities. The mean liquid mass fraction is therefore given by $\tilde{Y}$. On the right hand side, $\bar{\rho}\widetilde{u'Y'}$ represents the diffusion flux between the phases. This term implies that a relative velocity exists between the phases, and must be closed. If turbulent mixing is assumed to be wholly dominant, this term may be closed using Fick's law of diffusion as in equation (4.2). The diffusion coefficient is taken as μ_t, the turbulent viscosity, over Sc, the Schmidt number.

$$\frac{\partial \bar{\rho}\tilde{Y}}{\partial t} + \nabla \cdot \left(\phi \tilde{Y}\right) = \nabla \cdot \left(\bar{\rho}\widetilde{u'Y'}\right) \tag{4.1}$$

$$\bar{\rho}\widetilde{u'Y'} = -\frac{\mu_t}{Sc}\nabla \tilde{Y} \tag{4.2}$$

As Vallet and Borghi describe, this may be an over-simplification in many cases. Instead, they propose using the transport equation of the diffusion flux. With this change, the effects of diffusion, interface production, and interface destruction are all accounted for. Demoulin et al. expanded upon this approach to improve the performance of the model in regions with increased diffusion [25]. This is an important addition for liquid-gas multiphase flows where large inter-phase density ratios are inevitable. The closure, given by equation (4.3), exists as an option in the solver, but has not been tested thoroughly due to the non-linearities which it contains. The constant $C_p = 1.8$, k is the turbulent kinetic energy, ϵ is the turbulent dissipation rate, ρ_g is the gas density, and ρ_l is the liquid density. This is essentially the Fick's law

closure with an additional term to account for the effects of a high density ratio. The rest of Vallet and Borghi's model consists of a transport equation for the interfacial area density, Σ. This portion of the model was not used with this solver in the current work, and will be detailed in the next section.

$$\bar{\rho}\widetilde{u_i'Y'} = -\bar{\rho}\left[\frac{\nu_t}{Sc} + C_p\frac{k^2}{\epsilon}\bar{\rho}\left(\frac{1}{\rho_g} - \frac{1}{\rho_l}\right)\tilde{Y}(1-\tilde{Y})\right]\frac{\partial\tilde{Y}}{\partial x_i} \tag{4.3}$$

With the $\Sigma - Y$ model described and options for closure of the diffusion flux obtained, the rest of the solver is implemented as Garcia-Oliver et al. and Trask et al. detail [37, 113]. First, the liquid mass fraction is related to the density of the mixture by equation (4.4). To account for compressibility effects, equations of state must be used to determine each phase's density as the pressure changes. The ideal gas law is used for the gas phase (4.5), and a linear compressibility is used for the liquid phase (4.6). In these equations, p is the pressure, R is the specific gas constant, T is the temperature, ϕ_l is the liquid's constant compressibility, and p_0, ρ_0 are the liquid's reference pressures and densitities used for linearization. Isenthalpic flow is assumed for the cases in the current work, but a bulk enthalpy transport equation has been implemented and may be solved when necessary [113]. The temperature is then computed from the bulk enthalpy of the mixture to close the system.

$$\frac{1}{\bar{\rho}} = \frac{\tilde{Y}}{\rho_l} + \frac{1-\tilde{Y}}{\rho_g} \tag{4.4}$$

$$\rho_g = \frac{p}{RT} \tag{4.5}$$

$$\rho_l = \rho_0 + \psi_l\left(p - p_0\right) \tag{4.6}$$

These equations of state are sufficient for the continuity equation (4.7) to be closed via the chain rule using a volume averaged compressibility for the pseudo-fluid. The momentum equation (4.8) requires closure for the Reynolds stresses, which

is accomplished using a turbulence model. These equations are interpolated to faces and solved via a Pressure-Implicit with Splitting of Operators (PISO) algorithm [49]. Essentially, the velocity is predicted using the pressure from the previous timestep, and is then updated with a "corrector" once the new pressure is computed. This process is performed iteratively until convergence is achieved.

$$\bar{\rho}\nabla\cdot\bar{\mathbf{u}} = -\frac{\partial\bar{\rho}}{\partial\bar{Y}}\frac{D\bar{Y}}{Dt} - \frac{\partial\bar{\rho}}{\partial\bar{p}}\frac{D\bar{p}}{Dt} - \frac{\partial\bar{\rho}}{\partial\bar{T}}\frac{D\bar{T}}{Dt} \tag{4.7}$$

$$\frac{\partial\bar{\rho}\tilde{u_j}}{\partial t} + \frac{\partial\bar{\rho}\tilde{u_i}\tilde{u_j}}{\partial x_i} = -\frac{\partial\bar{p}}{\partial x_i} - \frac{\partial\bar{p}\widetilde{u_i'u_j'}}{\partial x_i} \tag{4.8}$$

4.2 HRMFoam

HRMFoam uses the $\Sigma - Y$ model in tandem with a phase change model to allow flash-boiling/cavitating channel flows and near-field sprays to be evaluated in a single simulation. The solver, initially developed by Gopalakrishnan and Schmidt [38], has been used extensively to model a variety of injection systems [67, 68, 66, 10, 32]. A detailed derivation of the solver is presented by multiple authors [38, 99, 79]. The governing equations will be summarized according to these works. First, the mass (4.9), momentum (4.10), and energy conservation equations (4.11) are introduced. Here, ϕ is the mass flux, $\vec{\bar{\tau}}$ is the stress tensor which includes turbulent effects, and h is the bulk enthalpy of the pseudo-fluid encompassing all three phases. Most of the flows in question are considered isenthalpic, but the enthalpy equation exists as an option in the solver, mostly to guarantee time accuracy if desired. The additional source term in the momentum equation, f, corresponds to an artificial drag force. This is part of a sealing algorithm, which will be introduced shortly.

$$\frac{\partial\rho}{\partial t} + \nabla\cdot\phi = 0 \tag{4.9}$$

$$\frac{\partial \rho \vec{U}}{\partial t} + \nabla \cdot \left(\phi \vec{U} \right) = -\vec{\nabla} p + \nabla \vec{\overline{\tau}} + \overline{f} \tag{4.10}$$

$$\frac{\partial \rho h}{\partial t} + \nabla \cdot (\phi h) = \frac{\partial p}{\partial t} + \vec{U} \cdot \nabla p \tag{4.11}$$

Next, it is useful to define the mixture density in terms of the fuel quality, x, the non-condensable gas (NCG) mass fraction, y, and the densities of the liquid fuel (ρ_l), fuel vapor (ρ_v), and gas (ρ_g) as in equation (4.12). The liquid and vapor densities are looked up in a pre-processed table based on the pressure and enthalpy for every cell. This table is generated using NIST's REFPROP application [58].

$$\rho = (1-y)(1-x)\rho_l + (1-y)x\rho_v + y\rho_g \tag{4.12}$$

This equation of state, however, is not sufficient to close the system due to the non-equilibrium nature of the phase change. In other words, because the time scale of the phase change cannot be ignored, the instantaneous and equilibrium fuel qualities are not necessarily the same. The Homogeneous Relaxation Model (HRM), proposed by Bilicki and Kestin [14], states that the rate of change of the fuel quality is governed by the instantaneous quality (x), the equilibrium quality ($\bar{x}$), and a relaxation timescale (Θ), as illustrated by equation (4.13).

$$\frac{Dx}{Dt} = \frac{\overline{x} - x}{\Theta} \tag{4.13}$$

The equilibrium quality is looked up from the REFPROP table, but the relaxation timescale must be modeled. Downar-Zapolski et al. produced empirical correlations for Θ by analyzing Reocreux's "Moby Dick" experiments of flash-boiling flow of water through a converging-diverging nozzle [29]. Saha et al. recently produced new correlations which tune the HRM to GDI sprays [94], but these have not yet been tested with the current solver. Downar-Zapolski et al. provide separate correlations

for upstream pressures below or above a transition value of ten bar. Both correlations relate Θ to the vapor volume fraction, α, and a non-dimensional pressure. In the low pressure correlation, given by equation (4.14), the pressure, ψ, is solely a comparison between the local and saturation pressures. In the high pressure correlation, given by equation (4.16), the fluid's critical pressure is also included, and the non-dimensional pressure is labeled φ. All case studies in the present work will use the high pressure correlation, unless the low pressure correlation is explicitly specified.

$$\Theta_{LP} = 6.51 * 10^{-4} \alpha^{-0.257} \psi^{-2.24} \tag{4.14}$$

$$\psi = \left| \frac{p_{sat} - p}{p_{sat}} \right| \tag{4.15}$$

$$\Theta_{HP} = 3.84 * 10^{-7} \alpha^{-0.54} \varphi^{-1.76} \tag{4.16}$$

$$\varphi = \left| \frac{p_{sat} - p}{p_{crit} - p_{sat}} \right| \tag{4.17}$$

The effects of compressibility and turbulent mixing may now be closed similarly to CoSigmaY. The liquid and vapor phases are both assigned a linear compressibility, and the NCG compressibility is computed using the ideal gas law. The overall mixture compressibility is a volume average of the compressibilities of each phase. The transport equation for y is the same as equation (4.1), but with the opposite sign on the right hand side. This accounts for the fact that the NCG mass fraction is the complement of the indicator function used in the previous section. The expression for the mixture density is then expanded via the chain rule as seen in equation (4.18)[10]. This expression is then combined with the discretized momentum equation and the continuity equation, allowing iterative solution via a PISO approach as detailed by [99]. The thermodynamic properties are updated at each timestep.

$$\frac{D\rho}{Dt} = \left.\frac{\partial \rho}{\partial p}\right|_{x,h,y} \frac{Dp}{Dt} + \left.\frac{\partial p}{\partial x}\right|_{p,x,y} \frac{Dh}{Dt} + \left.\frac{\partial p}{\partial y}\right|_{p,h,x} \frac{Dy}{Dt} \tag{4.18}$$

Mohapatra et al. recently added a sealing algorithm to the solver, allowing needle opening/closure events to be modeled [64]. When the needle's vertical displacement from its seat falls below a user-specified threshold, an artificial drag force is applied to cells within a user-defined bounding box. This allows pre and post-injection dynamics, multiple injections, and accurate initial conditions to be simulated without expensive topology changes. This drag force, which is added to the momentum equation as a source term as previously described, is defined in equation (4.19). Here, S_f is named the sealing factor, and S_d is a drag constant. The sealing factor, defined in equation (4.20), gradually trends towards the seal constant, S_∞, based on a time relaxation factor τ. This avoids the spurious water hammer effects which would arise from discontinuous changes in the drag force. When sealing is activated, the seal constant is set to unity for cells within the bounding box. In all other situations, the seal constant is zero.

$$\bar{f} = \rho \vec{U} \frac{S_f}{S_d} \tag{4.19}$$

$$\bar{S_f} = S_\infty \left(1 - e^{-\left(\frac{t}{\tau}\right)}\right) \tag{4.20}$$

CHAPTER 5

PRELIMINARY CASE STUDIES

5.1 Impinging Jet Sprays

The CoSigmaY solver was used to simulate the spray from a like-doublet impinging jet injector. X-Ray radiography experiments by Halls et al. were used to validate the results [41]. The injector had an enclosed an angle of 60 degrees, orifice diameters of $0.51mm$, and length-to-diameter $\left(\frac{L}{D}\right)$ ratios of 47. The $\frac{L}{D}$ of the free jets before the point of impingement was approximately 6. The experiments consisted of water injected into quiescent air at velocities of 30, 60, and $90m/s$, resulting in a Reynolds number range of $5,200 - 15,500$.

The experiments measured the equivalent path length (EPL) of liquid, essentially projecting the 3D liquid volume fraction (LVF) onto a 2D plane by integrating along the path of the X-Ray beam. The measurements were taken from two vantage points. The first scanned the major axis of the spray such that the jets were superposed on one another, as the visible light image shown in Figure 5.1 illustrates. The injector was then rotated 90 degrees to scan the minor axis of the spray, thereby allowing each free jet to be captured separately. Extracting the peak EPL location from each free jet allowed the jet crossing point to be accurately determined via trigonometry. Accurate and precise knowledge of this location is essential, as it allows the origins of the computational and experimental domains to be matched for quantitative comparisons.

Three computational grids were created for the simulations, with cell counts ranging from 580 thousand to 2.9 million. This enabled a grid dependence study, which

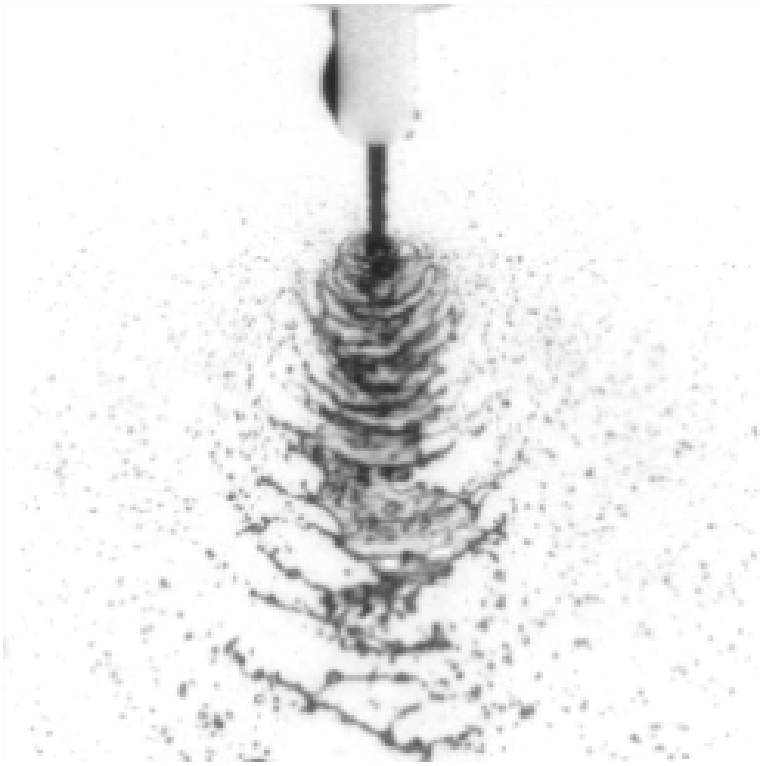

Figure 5.1: Visual light image of the impinging jet spray used in the experiments, reproduced from [50]. $Re = 10,300$.

revealed slightly better peak EPL predictions as mesh resolution increased (see Figure 5.2). The remaining simulations were performed using the high resolution mesh only. Each grid took advantage of the two symmetry planes in the geometry to simulate only a quarter of the domain, resulting in a 75% reduction in cell count. Local refinement was used to provide adequate resolution near the point of impingement while ensuring the overall cell count remained manageable. Figure 5.3 shows one of the grids used in the study. Nominally second order TVD flux limited schemes were used to ensure stability. The $k-\omega$ SST turbulence model was used, with a turbulent intensity of 2% applied at the liquid inlet and wall functions applied to the nozzle surface. The computations were performed until a quasi-steady state was observed.

The steady state results were then extracted for post-processing. First, a grid of sample lines was created in the simulation domain. The LVF values were then

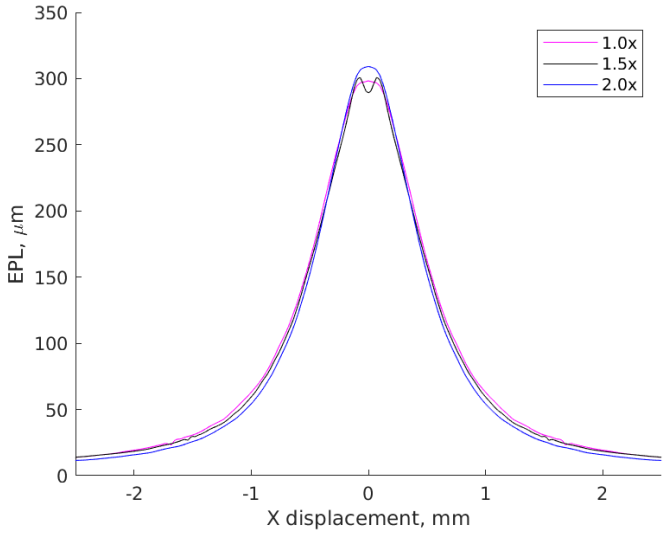

Figure 5.2: Grid dependence study results based on a sample plane $0.59mm$ downstream of the impingement point. The predicted peak EPL rises slightly with the mesh resolution. The dip near the center of the spray in the middle resolution case is likely an artifact caused by the symmetry boundary condition.

integrated along each line, yielding a field of EPL values. The computed EPL was doubled and mirrored about the impingement plane to reconstruct the full domain. Figures 5.4,5.5, and 5.6 compare the computational and experimental EPL results at various locations downstream of the jet crossing point. The EPL closest to the impingement point is predicted very well, which suggests that the thickness of the liquid sheet is being captured accurately. The EPL towards the center of the spray is consistently under-predicted further downstream, but the agreement improves towards the edges. The overall trends improve as Re, and consequently We, increase. This improvement suggests that the model would be well-suited for combustion-relevant conditions, particularly when the spray becomes supercritical.

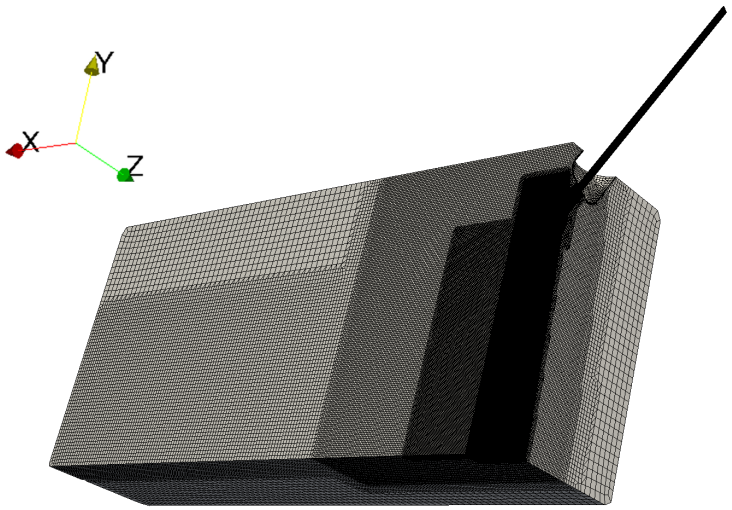

Figure 5.3: Example impinging jet spray mesh showing areas of local refinement.

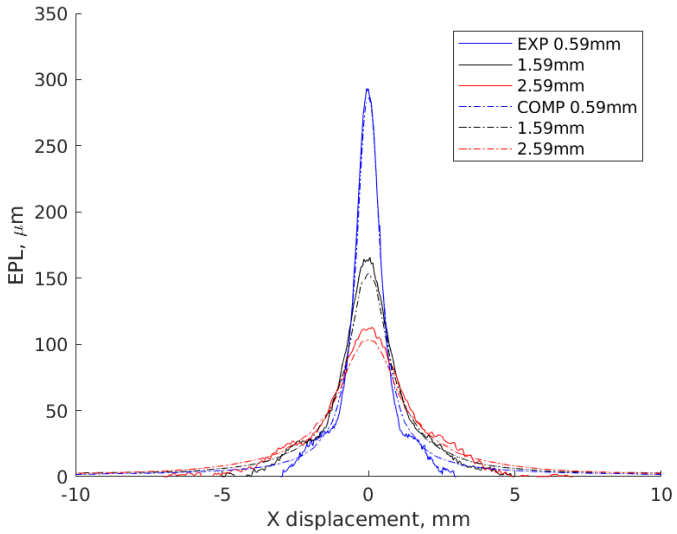

Figure 5.4: EPL vs. Horizontal position at various downstream displacements, $30 ft/s$. The origin is calibrated to the jet crossing point. Experimental data was limited to the near-field for this flowrate.

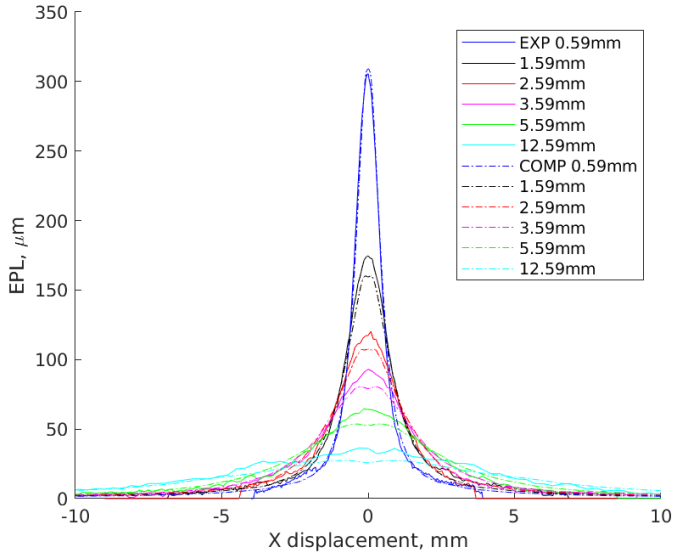

Figure 5.5: EPL vs. Horizontal position at various downstream displacements, $60 ft/s$.

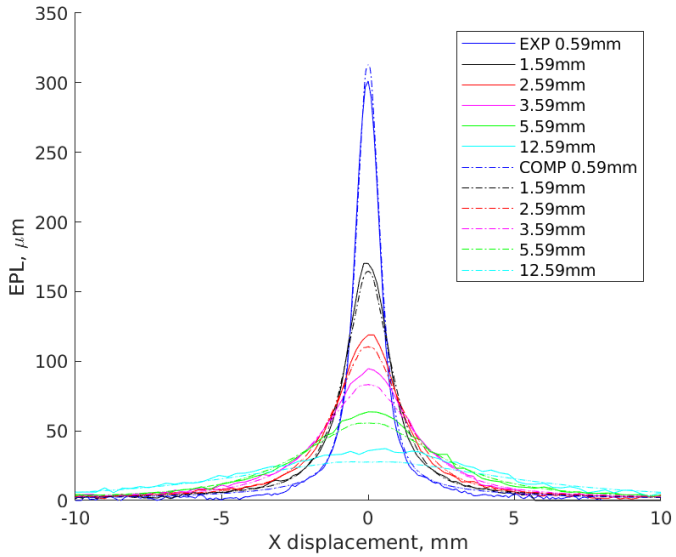

Figure 5.6: EPL vs. Horizontal position at various downstream displacements, $90 ft/s$.

5.2 Gasoline Direct Injection: RANS/LES Comparison

5.2.1 Overview

The transient vortices (see Figure 3.11) captured by Baldwin et al. are highly dependent on turbulence modeling [10]. The Baldwin et al. simulations used an Unsteady Reynolds Averaged Numerical Simulation (U-RANS) approach, which essentially time-averages the Navier-Stokes equations and adds a modeled fluctuating component to the velocity. RANS methods struggle to capture transient phenomena such as transition and flow separation, but are nevertheless the standard for industrial CFD simulations [44]. Spalart and Venkatakrishnan note that this is likely to remain the case for the forseeable future, and warn against over-confidence in such methods and even CFD in general [105]. Large Eddy Simulation (LES) is an increasingly popular alternative to RANS. LES spatially averages the spray, effectively using the mesh size as a low-pass filter for the Navier-Stokes equations. Features with length scales greater than that of the mesh are directly resolved, while "sub-grid scale" (SGS) stresses are modelled. While LES is still not practical for high-volume industrial usage due to its much higher mesh resolution requirements, it outperforms RANS for many flows, particularly those where separation occurs [13, 17, 21, 59, 86, 96, 111].

This case study will investigate the effects of turbulence modeling on GDI simulations with moving needles. RANS and LES Spray G simulations will be performed under identical operating conditions to draw direct comparisons between the two approaches. The RANS simulations will use the standard OpenFOAM implementation of the $k-\omega$ SST model [43, 62, 63]. The LES simulations will use the OpenFOAM implementation of the one-equation eddy model [56], with the SGS viscosity portion of the model replaced with the WALE approach proposed by Nicoud and Ducros [69]. The WALE model uses the square of the velocity gradient tensor to model the SGS stresses, and performs well in wall-bounded flows without the need for a dynamic LES approach [69]. Nominally second order Gamma differencing schemes were used

in all simulations. Finally, the Foam-Extend tetFEM library library was used for mesh motion [51].

First, a static needle grid dependence study will be performed using the as-designed, or "Generation 1", geometry to ensure adequate resolution is used for the moving needle simulations. The moving needle cases will use a geometry with modified dimensions based on X-Ray measurements of individual holes of the Spray G #28 injector. This "Generation 3" geometry, in addition to the as-designed geometry, are available via the ECN website [2]. The moving needle simulations will be compared against experimental data previously published by Duke et al [33]. These data were also used for simulation validation by Strek et al [107]. The standard Spray G operating conditions will be used for the grid dependence study, while slightly modified conditions will be used in the moving needle cases to match the experimental setup at ANL. Table 5.1 summarizes these conditions.

Table 5.1: Operating condition summary.

Property	Spray G	ANL
Injection Pressure	20 MPa	19 MPa
Back Pressure	600 kPa	315 kPa
Fuel	Iso-Octane	Viscor
Ambient Gas	Nitrogen	Nitrogen
Fuel Temperature	90° C	25° C
Ambient Temperature	300° C	20° C

Five computational domains were created. Three grids with increasing resolution were created using OpenFOAM's SnappyHexMesh for the mesh sensitivity study, with the needle placed at the default $45\mu m$ lift present in the Generation 1 geometry. Two refinement levels were used, as illustrated by the sample static mesh in Figure 5.7. The region upstream of the needle seat was omitted for simplicity and cost savings, as the thin sections near the needle guides required several extra refinement levels to

mesh successfully. The grids for the RANS and LES moving needle cases were then generated using Star-CCM+, as it handles such thin regions without significant user intervention. Starting the moving needle simulations with a very low needle lift is desirable, as it minimizes the discrepancy between the simulation and experimental start times. However, meshing at very low lifts causes a large increase in the cell count. To circumvent this, the mesh was created with the needle at $10\mu m$ of lift, with dynamic mesh motion subsequently applied to move the needle to its starting position of $2.5\mu m$. Figures 5.8 and 5.9 present samples of the moving needle meshes. Finally, Table 5.2 summarizes the cell sizes for all five grids. The first three rows refer to the static meshes, and the last two describe the moving needle meshes.

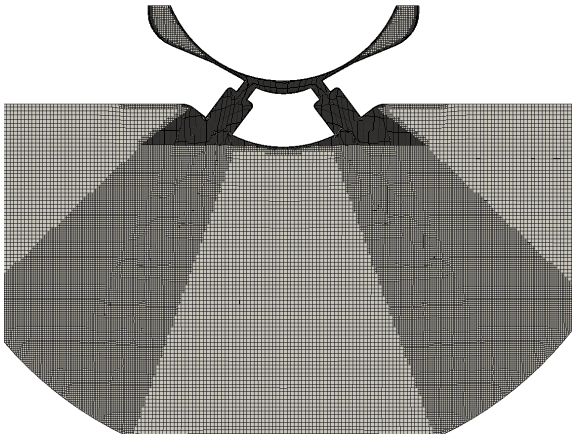

Figure 5.7: Sample of the "$4x$" resolution static needle mesh.

Table 5.2: Summary of mesh sizing statistics.

Mesh	Cells (Millions)	Nozzle Refinement	Downstream Refinement
1x	2.90	$18\mu m$	$36\mu m$
2x	5.57	$14\mu m$	$28\mu m$
4x	11.01	$11\mu m$	$22\mu m$
RANS	3.02	$10\mu m$	$40\mu m$
LES	7.72	$6.25\mu m$	$25\mu m$

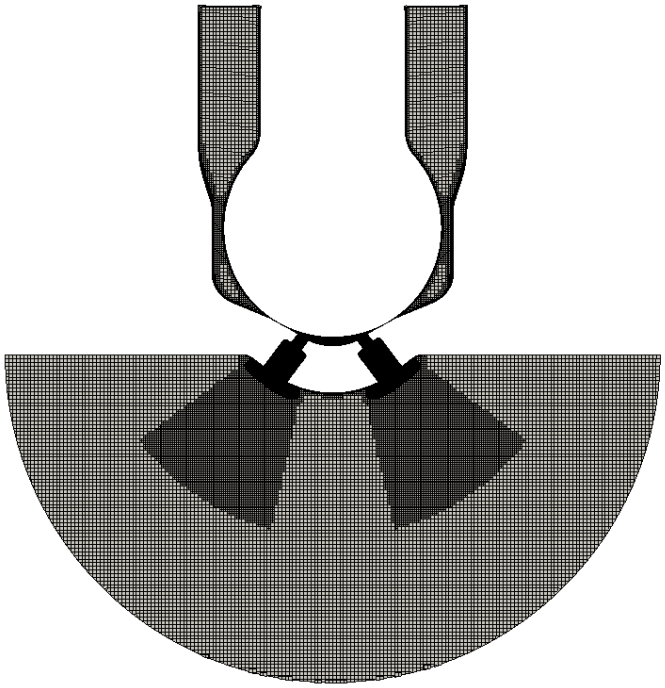

Figure 5.8: Sample of the LES moving needle mesh.

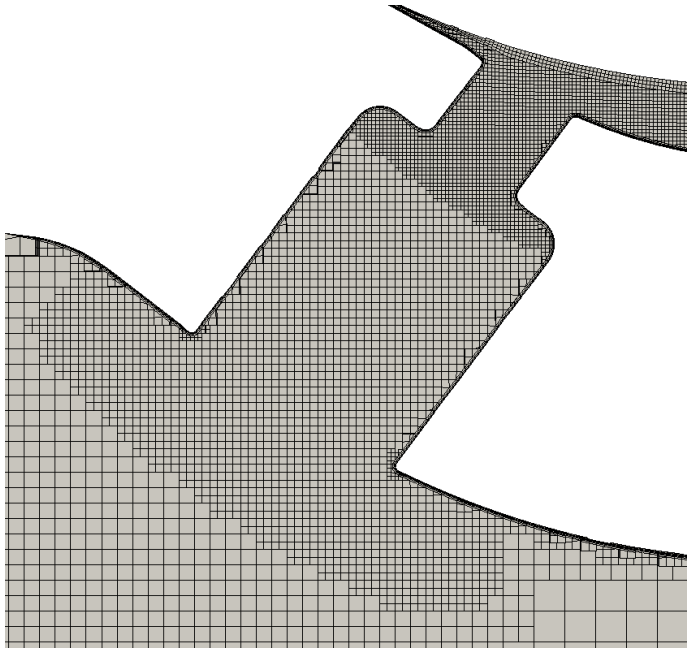

Figure 5.9: Detail view of the LES dynamic mesh. Three refinement levels are visible, and the extremely thin boundary layer cells on the nozzle walls are discernable.

5.2.2 Results: Grid Sensitivity Study

The results of the grid sensitivity study will now be presented. Grid sensitivity was evaluated in terms of mass flow rate convergence and contours of the fuel mass fraction for both RANS and LES. Pope suggests that the SGS kinetic energy should make up no more than 20% of the total kinetic energy in an adequately resolved LES computation, so the LES cases were also evaluated in terms of this metric [78]. Given the absence of an ensemble average, the velocity at each timestep was compared to a time-averaged velocity. Figures 5.10 and 5.11 present mass flow rate time histories for the RANS and LES cases respectively. The flow rates remain largely unchanged as the mesh resolution increases, suggesting that the results are converged by this metric. The inital fluctuations are a consequence of acoustic pressure waves due to the large pressure gradient imposed as the initial condition. The frequency of these pressure waves appears to change with the mesh resolution for the RANS cases, but the LES frequencies appear steady. This highlights the superior time accuracy of LES compared to RANS.

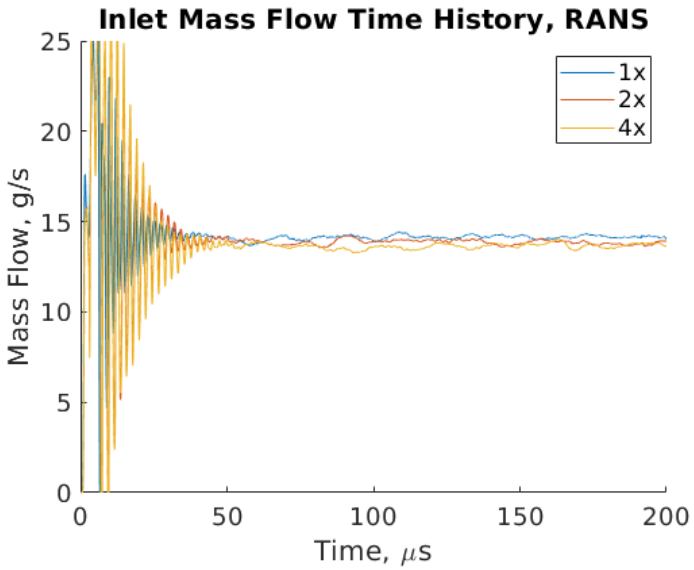

Figure 5.10: Static RANS mass flux results. Legend entries refer to the mesh used (see Table 5.2).

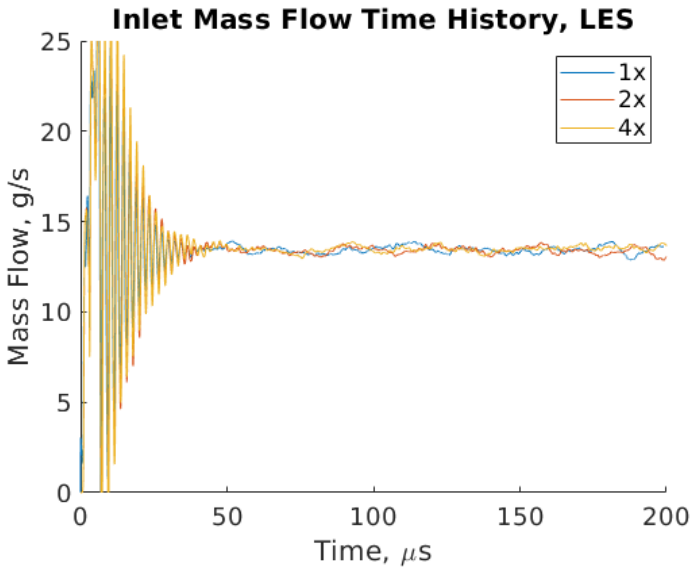

Figure 5.11: Static LES mass flux results. Legend entries refer to the mesh used (see Table 5.2).

Next, Table 5.3 shows time-averaged fuel mass fraction contours for the minimum and maximum grid resolutions. The results here appear relatively steady, with the spray cone angle largely unchanged as the cell sizes decrease. The distribution of fuel between the plumes changes slightly for the LES cases, but a longer runtime would likely reduce such discrepancies. RANS predicts far more entrainment of nitrogen into the counterbores than LES. Examining the LES cases reveals that gas entrainment was highly transient, suggesting that RANS is failing to capture important time-resolved phenomena.

Finally, the average Pope criterion is presented in Figure 5.12 for the $4x$ resolution LES case. The nozzle walls, counterbore walls, and inlet corners appear significantly under-resolved by this metric. The lower resolution cases (not pictured) exhibited progressively worse performance in these regions. This is unsurprising, as the resolution requirements of LES increase drastically near walls. An order of magnitude reduction in the cell sizes is likely necessary to achieve proper resolution of the boundary layer and satisfy this criterion, but the cost of such a reduction would be tremendous. As

Table 5.3: Time-averaged fuel mass fraction contours for the RANS (left) and LES (right) static cases, $1x$ (upper) and $4x$ (lower) resolutions.

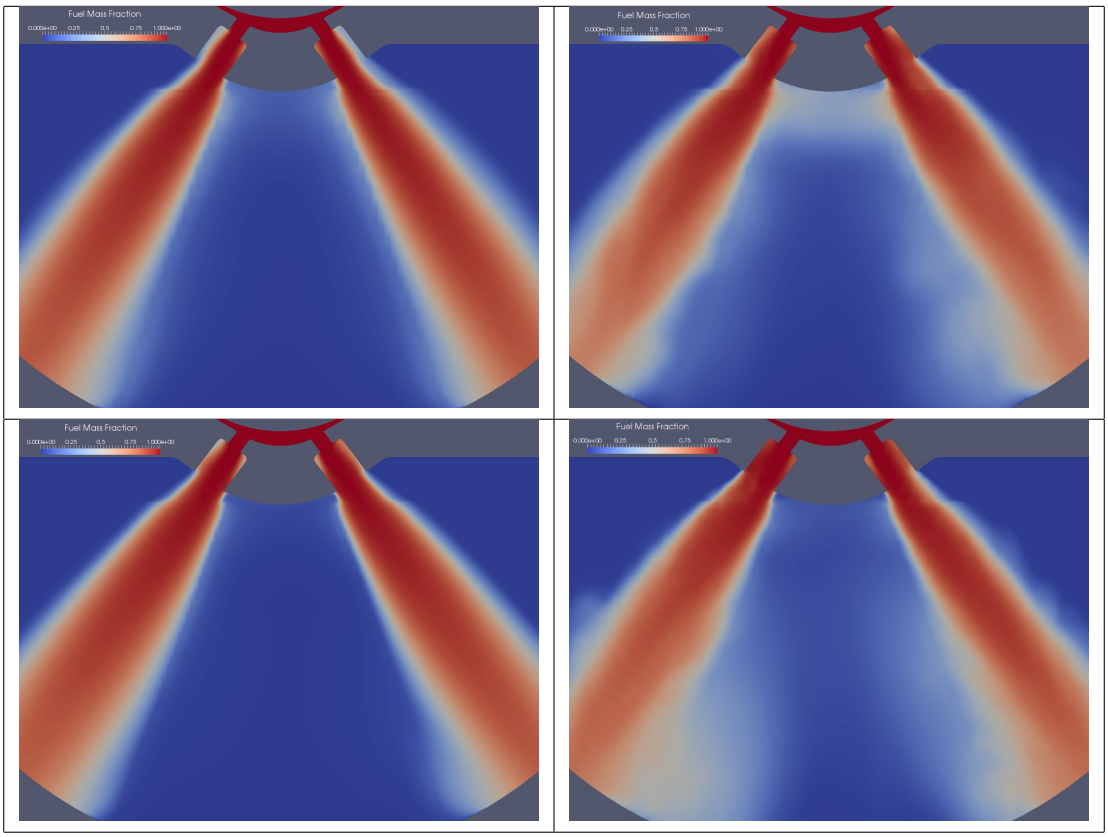

a compromise, an additional level of refinement was awarded to the wall-bounded portions of the geometry for the moving needle cases. Nevertheless, the results of the grid dependence study are promising overall, as no macroscopic changes in behavior were noted as the resolution increased.

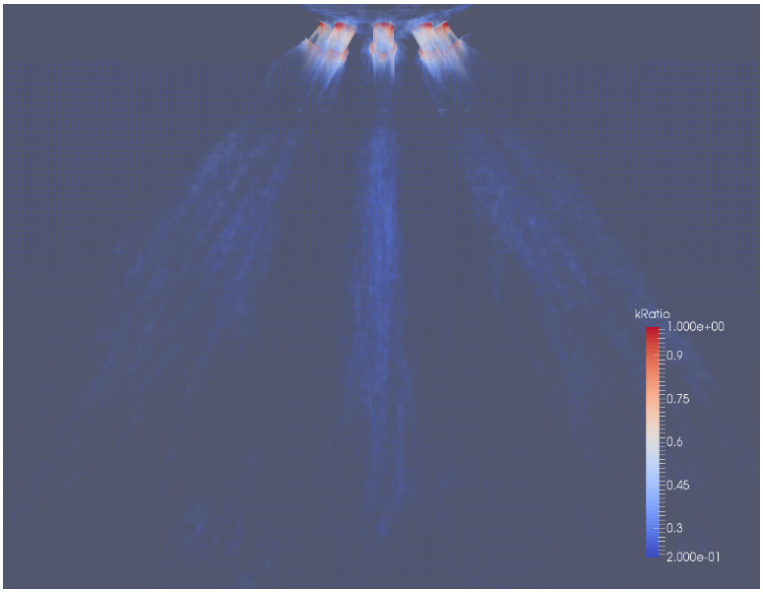

Figure 5.12: Pope criterion results, "$4x$" resolution LES case. $kRatio$ represents the fraction of the total (SGS and resolved) kinetic energy generated by the SGS model.

5.2.3 Results: Moving Needle Simulations

The moving mesh simulations were performed once cell sizing was selected based on the results of the grid dependence study. The $680\mu s$ needle motion profile from the ECN website [2], including both lift and wobble motion, was used to actuate the injection. The sealing algorithm was disenganged when the needle lift exceeded $2.6\mu m$ of total lift, or $0.1\mu m$ greater than the initial lift. End times for the simulations were placed shortly after SOI effects dissipated, allowing a short portion of the quasi-steady injection phase to be captured without the expense of a full duration computation.

Figure 5.13 compares the simulated ROI with the X-Ray radiography and long tube meter data. The long tube data are based on Spray G operating conditions, and are therefore included only for reference (see Table 5.1). Both simulations track the radiography measurements relatively well as a whole, with the LES results providing marginally better agreement. The simulated ROI was computed by measuring the flux through the nozzle holes, whereas the radiography data tracked the rate of change

of the fuel in the measurement area. This results in the apparent early ramp-up of the simulated ROI, as the fuel must continue through the counterbores and past the injector tip before being picked up by the radiography measurements.

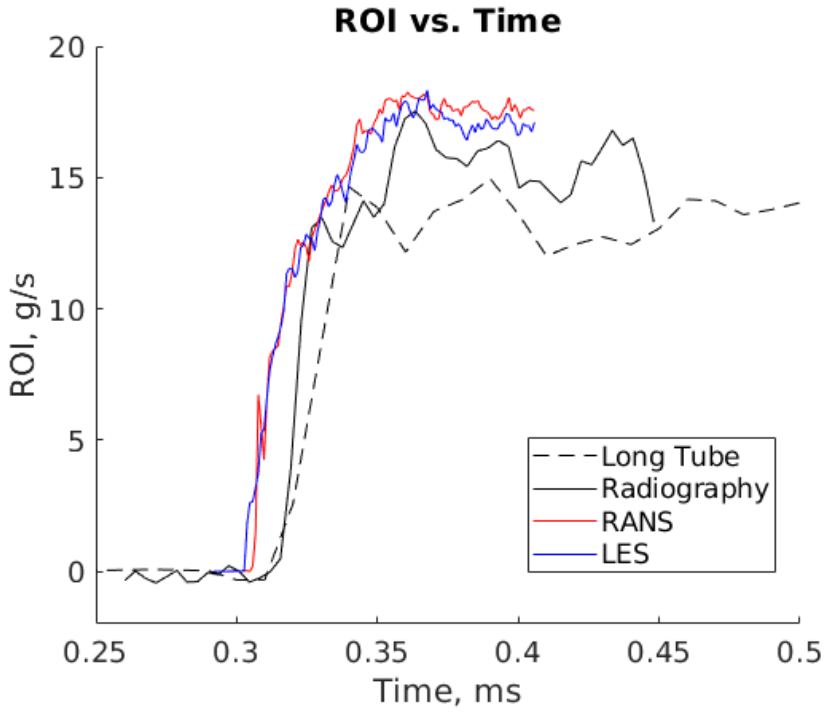

Figure 5.13: Comparison between the simulated and experimentally measured ROI for the moving needle simulations. Time is relative to the commanded start of injection (CSOI).

Next, the simulated projected mass is compared with the radiography data. The projected mass is essentially the mass per unit area in the path of the X-Ray beam, much like the EPL measurements in the previous section. However, in this case the fuel density is integrated in the CFD post-processing, as opposed to the LVF used in the previous section. Figure 5.14 presents the projected mass at a time of $407\mu s$ after CSOI.

Both RANS and LES predict the spray cone angle and qualitative jet structure relatively well, with LES performing slightly better in terms of capturing separation between the plumes. However, both simulations over-predict the projected mass in

the near-field region and under-predict the fuel penetration. The CFD post-processing allows for a much higher sampling resolution, which may contribute to the near-field discrepancy. The external spray results may also be influenced by the proximity of the outlet boundary, as a $9mm$ diameter hemispherical plenum was used. This places the outlet boundary just over $3.5mm$ downstream of the injector tip, which may affect air entrainment patterns, pressure values, and penetration predictions in the simulated external spray domain.

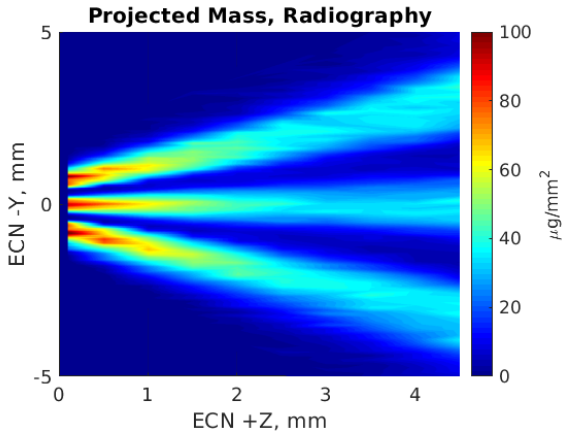

(a) Radiography projected mass measurement

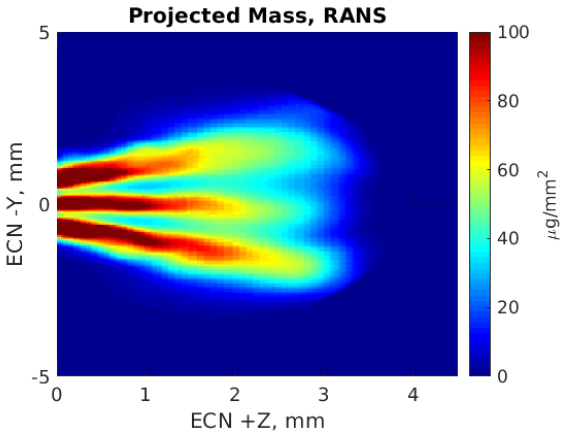

(b) RANS simulated projected mass

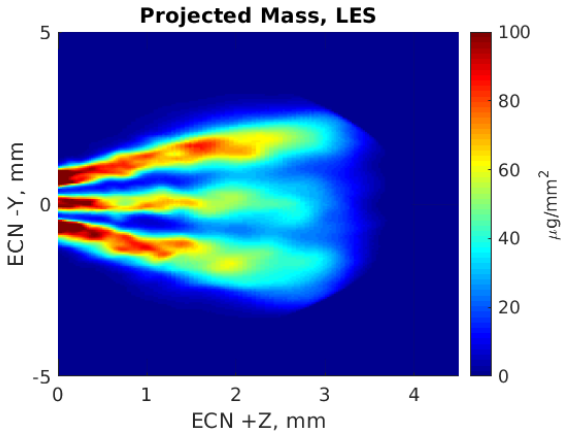

(c) LES simulated projected mass

Figure 5.14: Projected mass comparison at $t = 407\mu s$.

Figure 5.15 compares density results at a location of $z = 2mm$ in ECN coordinates, effectively $2mm$ downstream from the injector tip. RANS predicts the qualitative

structure of the plumes with some success, although the plumes appear to be too diffuse. The LES results are quite different, displaying sharp, asymmetric plumes. These structures have been observed in time-resolved X-Ray measurements [34]. The experimental data currently being referenced were ensemble averaged over 30 injection events [33], so the plumes appear to share more simularities with the inherently time-averaged RANS data. Time averaging these sample planes over a full-duration injection event would likely yield better results. The outside edges of the plumes are close to the domain limits this far downstream, implying that proximity of the outlet boundary adversely affects these results as well.

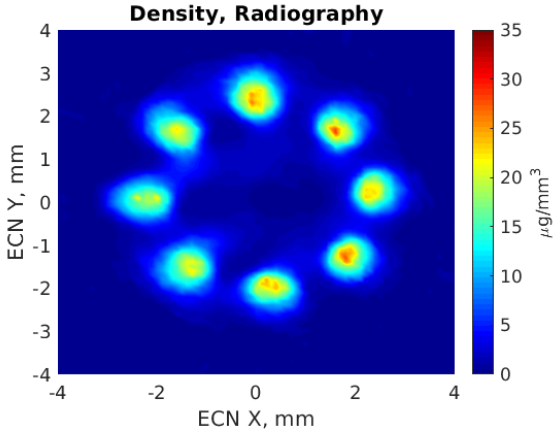

(a) Radiography sample plane

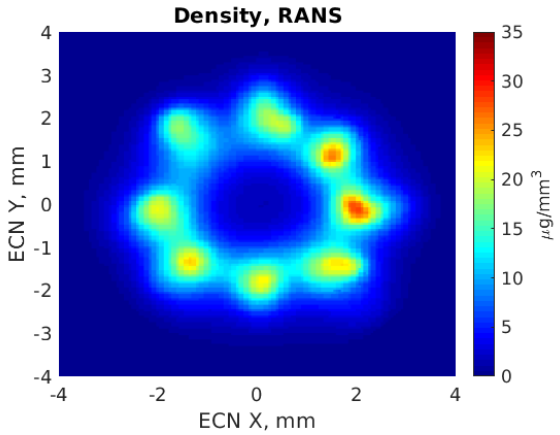

(b) RANS sample plane

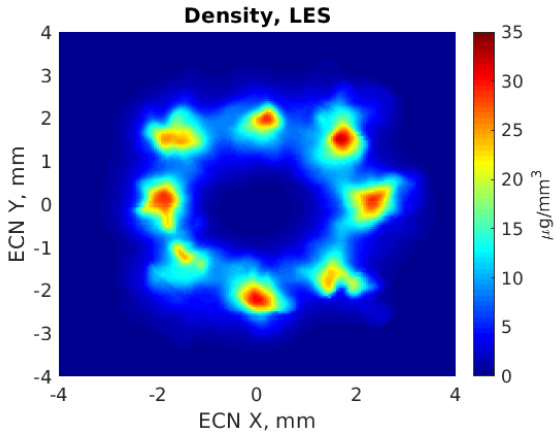

(c) LES sample plane

Figure 5.15: Density sample plane comparison at $t = 407\mu s$, $z = 2mm$.

Finally, the turbulent vortices were visualized according to the process used by Baldwin et al. [10]. Total pressure isosurfaces were created at $14MPa$ and colored by static pressure, as seen in Figures 5.16 and 5.17. The RANS vortices are qualitatively similar to those predicted by Baldwin et al., whereas LES predicts a higher number of smaller, more chaotic structures. These differences would likely yield discrepancies in per-hole ROI between the two approaches over a full injection duration, but would not cause macroscopic changes. Vortex visualizations in terms of the Q and λ_2 criteria were also created [47], but the high number of small structures made it difficult to draw useful conclusions.

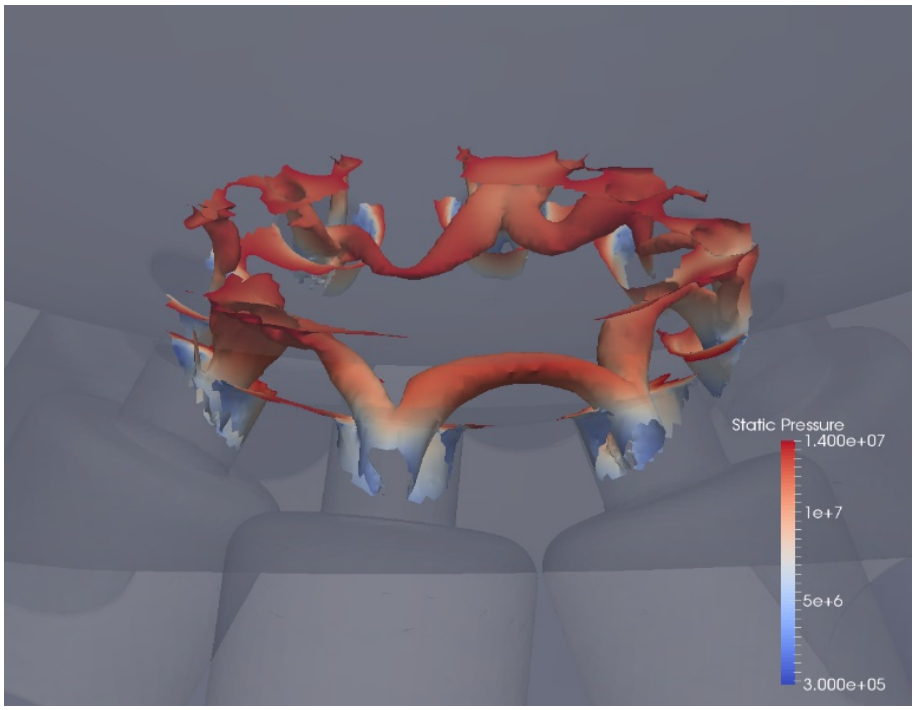

Figure 5.16: RANS turbulent vortices, $t = 407\mu s$.

In general, both RANS and LES performed adequately in terms of qualitative external spray characterization and quantitative ROI prediction. LES produced slightly more accurate results, likely due to its ability to resolve transient effects. Grid sensitivity analyses showed that while the LES results appeared converged in terms of

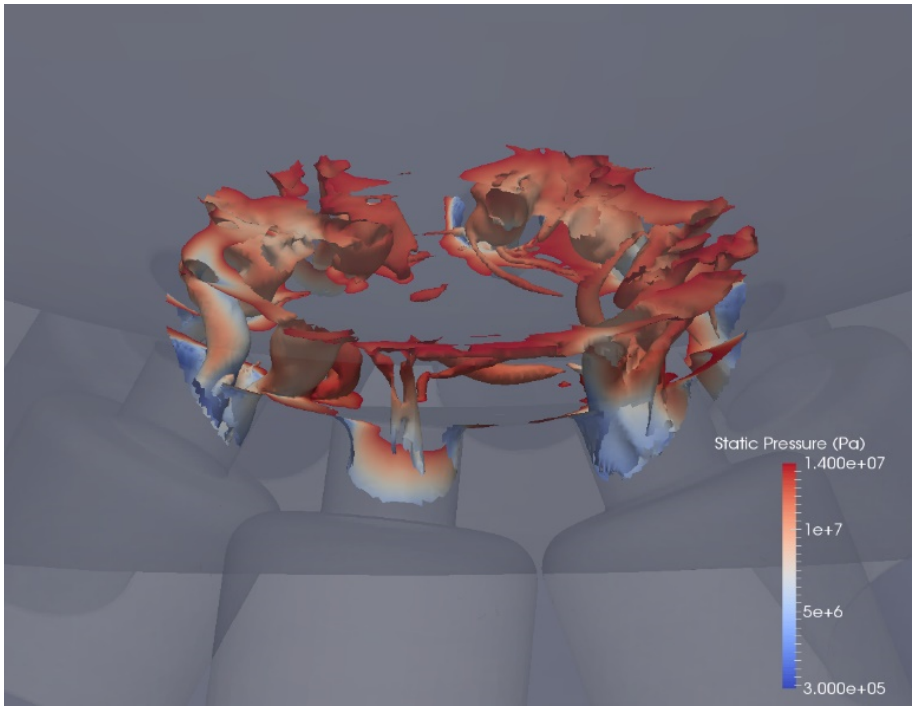

Figure 5.17: LES turbulent vortices, $t = 407\mu s$.

macroscopic phenomena, the wall bounded portions of the flow would require a large increase in cell resolution to properly resolve the boundary layers. Given the broad similarities between the results, LES may not warrant the cost premium it carries over RANS for moving needle GDI simulations.

5.3 Diffusion Flux Closure Effects

The previous section revealed that HRMFoam over-predicts the density of the fuel plumes just downstream of the injector tip. One possible contributor to this is the use of Fick's law of diffusion to close the diffusion flux term in the NCG transport equation. This term, reproduced in equation (5.1), governs the rate at which the fuel and gas mix, and thereby plays an important role in determining the downstream density distribution. This suggests that improving upon the basic Fick's law closure could improve the agreement between the simulations and experiments.

$$\bar{\rho}\widetilde{u'Y'} = -\frac{\mu_t}{Sc}\nabla\tilde{Y} \tag{5.1}$$

To test this hypothesis, the transport equation for the NCG mass fraction in HRMFoam was modified to use the Demoulin et al. closure discussed previously and reproduced in equation (5.2) for convenience. The Laplacian was solved using Foam-Extend's built in explicit nonlinear solution methods. A loop was included to solve the equation iteratively until the initial residual fell below a user-specified threshold. This ensured that the Laplacian for the current and next time steps were as consistent as possible, thereby increasing stability. Even so, initial tests revealed that the pressure solution became incredibly unstable with the modified NCG equation, especially in regions with large gradients in both pressure and NCG mass fraction. The NCG mass fraction is included in the pressure equation via the chain rule, so it is unsurprising that large gradients in both fields stress the solver. To combat this instability, the increase in diffusion due to the additional source terms was limited to two orders of magnitude greater than the diffusion predicted by the Fick's law closure. Determining a more physical limit would be worthwhile should the modified equation show promise.

$$\bar{\rho}\widetilde{u_i'Y'} = -\bar{\rho}\left[\frac{\nu_t}{Sc} + C_p\frac{k^2}{\epsilon}\bar{\rho}\left(\frac{1}{\rho_g} - \frac{1}{\rho_l}\right)\tilde{Y}(1-\tilde{Y})\right]\frac{\partial\tilde{Y}}{\partial x_i} \tag{5.2}$$

The modified and original solvers were both used on a typical static needle Spray G case to compare the performance of the two flux closures. The mesh and operating conditions used were identical to the "1x" U-RANS case used in the grid dependence study discussed in the previous section. The simulations were performed until a quasi-steady state was observed, at which point the solutions were time-averaged over a period of 50 microseconds. First-order upwinding schemes were used for advective terms. This represents a significant reduction in accuracy, but the increased stability allowed for larger timesteps and consequently shorter simulation runtimes. The goal

of the current case study is an apples-to-apples comparison of the two models, so this was deemed an acceptable tradeoff.

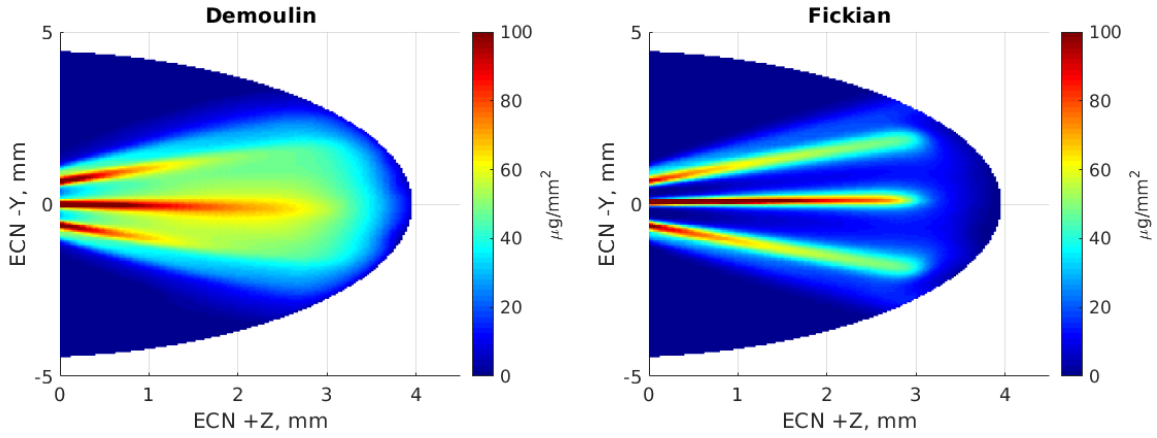

Figure 5.18: Average projected mass profiles for the Fick's law and Demoulin et al. diffusion flux closures.

Figure 5.18 presents the average projected mass predicted by both models. The plume structures are strikingly different than those of the previous study. The Fick's law closure case is identical to the "1x" U-RANS grid dependence simulation from the previous study except for the change in advection schemes, suggesting that the difference in plume structure is entirely due to the use of upwinding. The first notable difference between the two models is the increased amount of fuel between the plumes predicted by the Demoulin et al. closure. This does not constitute spray collapse, as the plumes appear fully separated just downstream of the injector tip. Nevertheless, the high density between the plumes is unrealistic. Investigating the magnitude of the diffusion flux term in the NCG mass fraction transport equation, as shown in Figure 5.19, shows that significant levels of diffusion occur in the center of the spray. No large density gradients exist outside of the plume boundaries, suggesting that the model is predicting an unrealistically high diffusion coefficient between the plumes. Taken as a whole, the Fick's law of diffusion closure appears to be simpler, more

stable, and more accurate than the Demoulin et al. closure, and it will therefore continue to be used in subsequent simulations in this work.

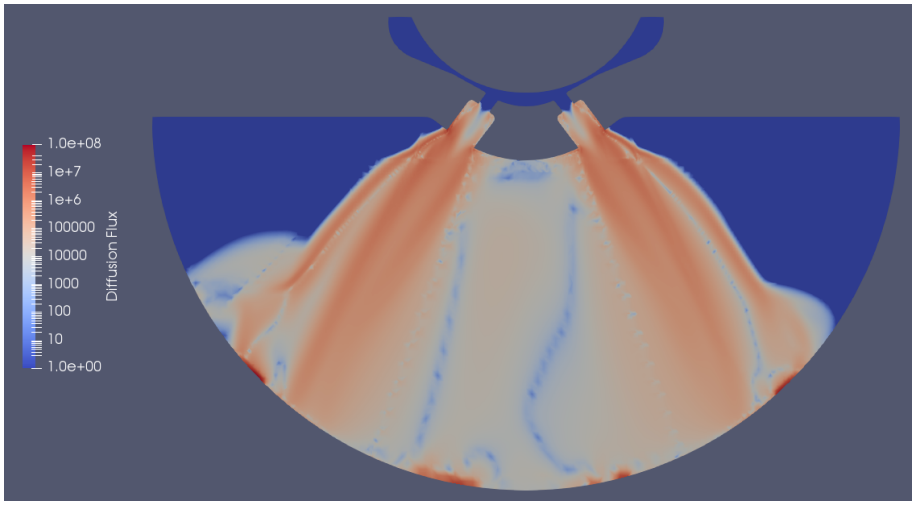

Figure 5.19: Cut plane of the instantaneous diffusion flux (Demoulin et al. flux closure) in the NCG mass fraction transport equation during quasi-steady state.

CHAPTER 6

MOVING MESH SIMULATION WORKFLOW

6.1 Motivation

Including as-manufactured geometry into future fuel injector simulations, the importance of which has been discussed in previous sections, requires a new mesh motion approach. Current methods rely on the tetFEM library within Foam-Extend [51]. This library decomposes each cell into tetrahedrons, assigns stiffness properties to each tet cell based on its quality metrics, and performs a finite element method calculation in conjunction with Laplacian smoothing to distribute the "loads" produced by the required motion. As Jasak and Tukovic demonstrate, this approach allows significantly higher mesh displacements to be reached before the mesh becomes degenerate [51]. This allows the full needle motion event, including both axial lift and off-axis wobble, to be simulated on a single mesh. However, the library has several limitations. First, it is highly dependent on having consistent cell types. It is expensive and difficult to decompose polyhedral cells with inconsistent shapes and high face counts. In internal tests, the library simply failed to converge for even a single timestep of motion for meshes generated with several packages. Tetrahedra and hexahedra appeared to be the most reliable cell types for convergence. This is problematic, as the complicated features present in as-manufactured geometries require modern, powerful meshing tools that utilize many cell types to be processed accurately and efficiently.

Next, even with a compatible mesh, the performance of the library is poor. To examine this, a comprehensive scaling study was performed using HRMFoam. A

mesh with 4.2 million hexahedral cells was used for all cases. The mesh was decomposed into 48, 96, and 144 cores, representing 1, 2, and 4 nodes of the Stampede 2 computing cluster where the study was performed. The compute nodes utilized two Intel®Xeon Platinum 8160 "Skylake" processors, each containing 24 cores at a nominal clock speed of 2.1GHz. The processors each have six memory channels and utilize AVX-512 instruction sets, both of which result in significant performance increases for CFD when compared with previous generations of Xeon processors. A fixed timestep of one nanosecond was set, and the endtime was set at 0.5 microseconds. This results in a benchmark test comprised of startup tasks, 500 simulation timesteps, and shutdown tasks. Data output was disabled for the simulations to omit the impact of IO performance as much as possible. A simulation was performed on each decomposed mesh, and the wall time was recorded as reported by Foam-Extend. The study was initially performed for a static-needle configuration, and was then repeated for the tetFEM library.

A third mesh motion library, the "displacementLaplacian" library in Foam-Extend, was also tested. This library moves points on a user-specified boundary based on an input table containing displacement and time information. The point displacements are then interpolated to cell centers, at which point a Laplacian is solved using a user-selectable motion diffusivity scheme to control the distribution of the motion. In this work, a new diffisivity was written which increases linearly with the distance from the specified boundary. In the context of a moving-needle fuel injection simulation, this results in most of the motion being absorbed by the cell layers closest to the needle. These are normally high quality, relatively uniform boundary layer cells, which stretch quite far before their quality is compromised. Once the Laplacian has been solved, the motion of the cell centers is interpolated back to the points, and the mesh is updated. This technique is much simpler, as it eliminates the need to decompose cells into tetrahedra and does not require finite element method solutions. However,

this simplicity does not come without cost, as cell quality deteriorates much faster than the tetFEM library for a given amount of needle motion. The consequences of this will be discussed shortly.

Figure 6.1 presents the results of the performance study in terms of elapsed wall time vs. node count for all three motion types. Table 6.1 quantifies the speedup in terms of percent of linear scaling, and also includes the computation of a "grind factor". Linear scaling refers to the notion that for an idealized parallel program, an additional one-hundred percent speedup would be achieved every time the number of processors is doubled. If this speedup were plotted on a log-linear scale versus the number of processing cores used, it would then appear to be linear. The grind factor allows the cost of the code to be quantified in terms of $\frac{CPUhours}{Cell*Timestep}$, and was computed based on the single node wall clock time to exclude the effects of network architecture. For the moving-needle cases, the needle was lifted at a steady $2\frac{m}{s}$ to achieve one micron of lift by the end of the simulation.

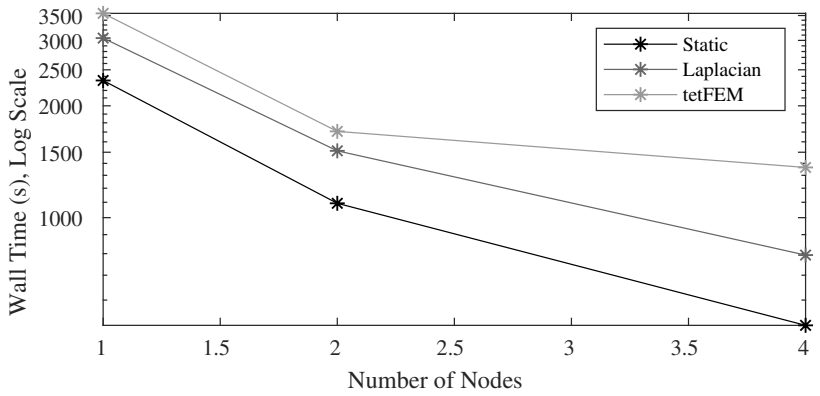

Figure 6.1: Benchmark test results.

The first notable result is that for all motion libraries, a super-linear speedup was achieved for the 2 node cases. The Stampede 2 "Skylake" nodes have a large cache capacity, with 114MB per node split between L2 and L3. As the simulation is decomposed across more nodes, more data can be accessed from cache, skipping the slow

Table 6.1: Benchmark test results.

Motion	Grind Factor	% Linear, 2 Node	%Linear, 4 Node
Static	$5.37e-5$	107%	114%
Laplacian	$6.98e-5$	101%	96%
tetFEM	$8.13e-5$	104%	64%

trip to main system memory which limits the performance of most CFD codes. The performance increase from this phenomenon is significant enough that it outweighs any losses due to inter-node communication, thereby achieving super-linear speedup. This continues for the 4 node static-needle case, while the displacementLaplacian library falls just below linear. The tetFEM library displays hardly any additional speedup compared to the 2 node case. This poor scaling is another weakness of the library. Previous attempts to run highly parallel cases with this library were unsuccessful, as the speedup trends towards zero quickly as the core count increases further. The tetFEM library also carries a higher grind factor than the displacementLaplacian library, which is unsurprising due to the significantly more complicated model. Given the results of this performance study, a new workflow to simulate as-manufactured geometries will be developed based on the displacementLaplacian motion library.

6.2 Geometry Preparation and Case Setup

The test geometry for this workflow is based on a preliminary X-Ray tomography reconstruction of the Spray G 28 injector, created by Dr. Brandon Sforzo at Argone National Lab. Key dimensions of the geometry are summarized in Table 6.2 based on documentation from the ECN website [2]. The geometry was truncated at the needle guides. This requires the inlet boundary condition to be enforced on the extremely thin section between the needle and the guides, which is problematic even for a static-needle simulation. In addition, the tomographically scanned needle was included, which would eliminate the possibility of placing uniform boundary layer

cells near the needle surface to encourage stable mesh motion. To overcome these challenges, the X-Ray geometry was trimmed 0.31mm above the ECN origin. The nominal geometry, obtained from the ECN website, was then cut in the same location. The two geometries were then stitched together using Blender's LoopTools plugin, as seen in Figure 6.2. The edge loops left over from trimming the geometry are selected, and faces added between them. The end result retains a smooth needle and seat region, allowing for much easier mesh motion convergence and boundary condition enforcement. The most difficult part of this process is manually aligning the nominal and experimental geometries, as any errors will alter the results of the simulation. Automatation of this process would be beneficial in the future.

Table 6.2: Summary of key nozzle dimensions (all units in microns).

Property	Hole 1	Hole 2	Hole 3	Hole 4	Hole 5	Hole 6	Hole 7	Hole 8	Design
Nozzle Diameter (Upstream End)	177	172	168	172	172	172	166	170	165
Nozzle Diameter (Downstream End)	177	172	172	175	175	172	170	172	165
Inlet Corner Radius	17	19	10	15	19	7	6	7	0

The next challenge posed by the X-Ray geometry was mesh generation. The extremely intricate and random surface features are quite difficult to mesh, and doing so with a typical block based approach is infeasible. In addition, to allow the entire needle motion event to be simulated, multiple meshes must be created. Since the displacementLaplacian library simply smooths the motion and does not attempt to maintain cell quality, periodic re-meshing is required as the needle is raised and lowered. The solution is then mapped from mesh to mesh as the simulation progresses. This is accomplished using the standard "mapFields" utilities that are available in both Foam-Extend and OpenFOAM. For the current work, the OpenFOAM 5 version of the utility is used, as it allows the user to select between multiple interpolation options. The method selected for the current simulations simply maps solution data

to the nearest cell of the new mesh. Mass conservation is not guaranteed using this method, but it was used for the present simulations due to its consistent stability during initial tests. The development of a more robust mapping method would benefit such workflows in the future.

This strategy essentially uses the meshing algorithm itself to maintain cell quality. While this is a much more pragmatic and less elegant approach than that posed by the tetFEM library, it is simpler to put into reliable practice, and allows for fast simulations on much larger and more complicated meshes. The accuracy of the mapping algorithm only affects the start and end of the injection event, as the majority of the injection is at a relatively steady lift and consequently remains on the same mesh. For the current study, the initial mesh was created at 10 microns of needle lift, with additional meshes used every subsequent 5 microns up to the needle's peak lift of 50 microns. A hemispherical spray plenum 20mm in diameter was used, much larger than the 9mm diameter plenum used in previous sections.

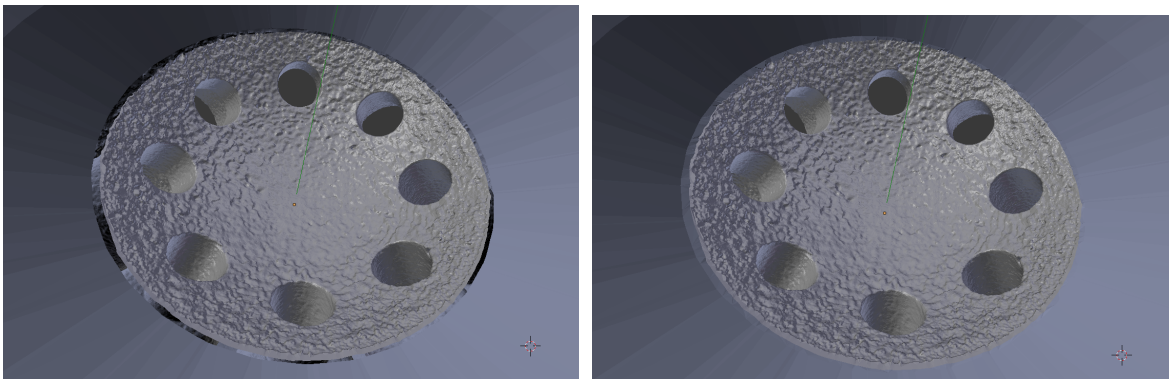

Figure 6.2: Visualization of the experimental and nominal geometries before and after stitching.

The initial mesh was created using the polyhedral, thin, and prism meshers in Star-CCM+, with the resultant mesh imported into OpenFOAM. This results in a very high quality mesh, especially in the thin needle seat region as seen in Figure 6.3. However, Star-CCM+ does not appear to accurately capture all surface features. In

addition, this combination of meshing algorithms must be run in serial, leading to a lengthy mesh generation process. The cell counts required to adequately resolve the nozzle regions were also quite high, with the final mesh containing approximately 3.1 million cells despite a relatively coarse section in the plenum and poor resolution of surface features.

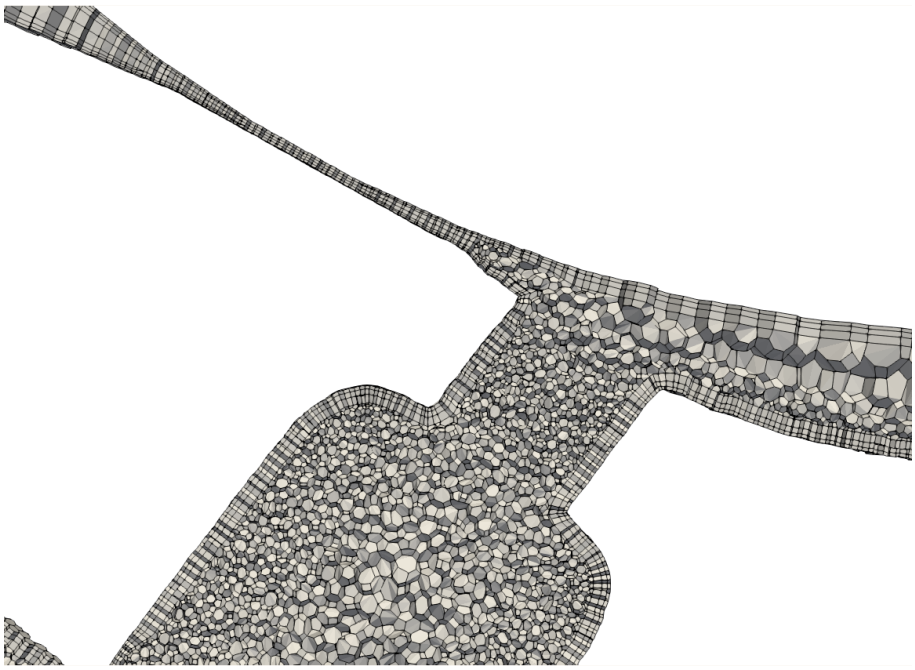

Figure 6.3: Sample view of the Star-CCM+ mesh for the Spray G 28 injector at 10 microns of needle lift. The polyhedral core cells, prism layer boundary cells, and special thin cells in the needle seat region are all visible.

The rest of the grids were generated using OpenFOAM's SnappyHexMesh, as the higher needle lifts were more suitable to its cut-cell method. This application is open source and highly parallelized, allowing for free and fast mesh generation on large numbers of processors. SnappyHexMesh also captures the intricate surface features quite well, as evidenced by Figure 6.4. The user specifies a maximum number of allowable octree refinements from the given base cell size on a given surface. SnappyHexMesh then refines the cells around the surface until the normals of adjacent faces align within a user-specified tolerance angle, or until the user-specified maximum re-

finement level is reached. Once the refinement is complete, the mesh displacement is smoothed until the cells fit the input surface as closely as possible. This allows small surface features to be resolved quite sharply (see Figure 6.5) without an unnecessary increase in global cell count, all with little effort on the part of the user. Finally, refinement regions were set in the spray plenum as seen in Figure 6.6. The refinement regions were identical for all of the SnappyHexMesh grids which were created. This alleviates a significant portion of the mass conservation concerns generated by the solution mapping, as the accuracy of mapping to the nearest cell on the new mesh is highest when the meshes are identical. Final cell counts were approximately 3.6-3.9 million cells depending on the needle lift.

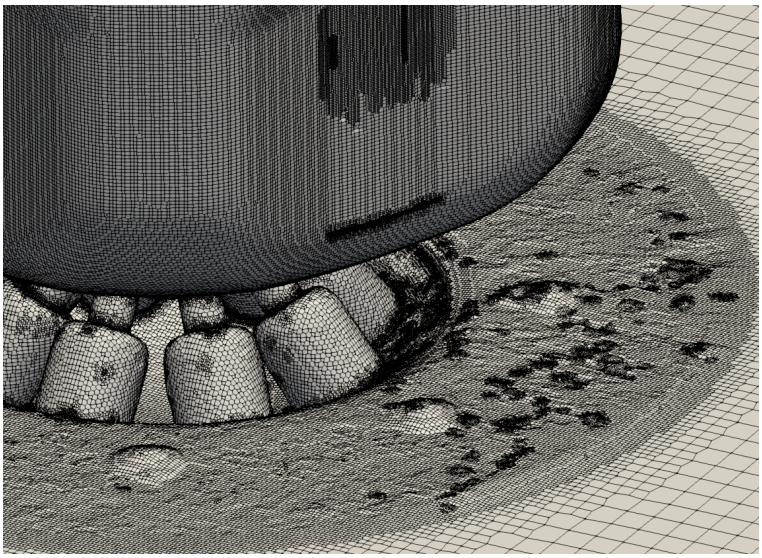

Figure 6.4: Outside view of a sample SnappyHexMesh grid, showing accurate capture of intricate surface features.

Finally, with mesh generation complete, an initial condition was developed for both of the operating conditions selected for testing. These comprised the ANL Spray G equivalent previously discussed, as well as a new ANL Spray G2 equivalent to match upcoming experiments of a flash boiling condition. These are summarized in Table 6.3. Fuel property data were generated generated using NIST's REFPROP software

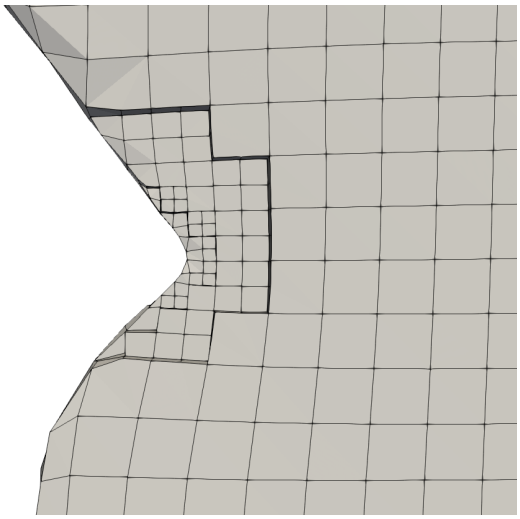

Figure 6.5: Detail view of a sample SnappyHexMesh grid near a nozzle to counterbore step, showing local refinement to capture the sharp region.

as before [58]. The ANL-G2 condition uses neat iso-octane, which is not doped with the Cerium contrast agent used for the ANL-G experiment. This removes the need to understand how the Cerium agent behaves when the fuel vaporizes, which will greatly simplify comparisons with flash-boiling simulations. For the current comparisons with the ANL-G experiment, it is assumed that the doping agent simply modifies the density and viscosity of the isotropic mixture. Vaporization is mostly limited to cavitation within the nozzle for this condition, so this is deemed an acceptable simplification.

In previous works, initial field values were set based on user input, often comprised of a hyperbolic tangent pressure ramp in the sac with a matching transition from fuel to NCG. This is not as realistic as possible, and can affect results such as the time for fuel to initially leave the injector at the start of injection (SOI) depending on how the sac is initialized. For the current work, the initial mesh at 10 microns of lift was initialized as usual and then simulated with a static-needle until a quasi-steady state was observed. The sealing algorithm was then manually triggered, simulating an end of injection (EOI) scenario. This is not a perfect representation of a full

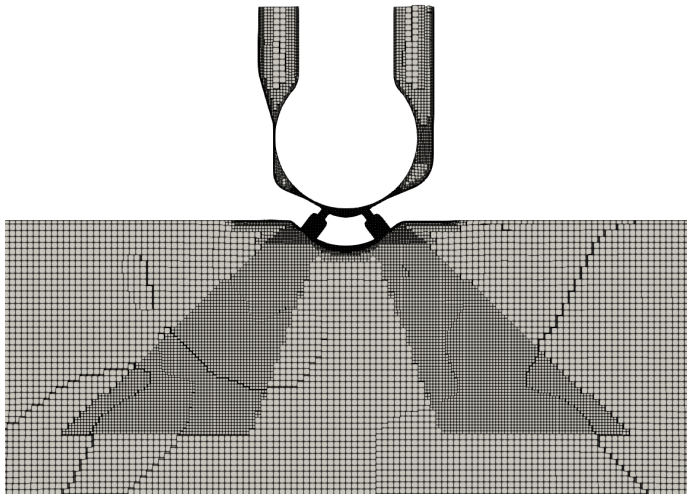

Figure 6.6: Downstream mesh refinement for the SnappyHexMesh grids.

injection event, as the needle is never raised to its proper lift, but it is nevertheless more realistic than assigning an arbitrary ramp to the pressure and fuel mass fraction fields. Figure 6.7 displays the fuel mass fraction initial condition for both simulations. A significant and asymmetric liquid fuel dribble is present for the G condition, while the G2 condition has a pool of fuel downstream of the injector. However, the G2 condition contains purely vapor downstream of the needle seat, suggesting that the entire sac has boiled off as shown in Figure 6.8.

Table 6.3: Operating condition summary.

Property	G	ANL-G	G2	ANL-G2
Injection Pressure	20 MPa	19 MPa	20 MPa	20.11 MPa
Back Pressure	600 kPa	350 kPa	50 kPa	50 kPa
Fuel	Iso-Octane	Viscor	Iso-Octane	Iso-Octane
Ambient Gas	Nitrogen	Nitrogen	Nitrogen	Nitrogen
Fuel Temperature	90°C	25°C	91.1°C	90°C
Ambient Temperature	300°C	20°C	60°C	60°C

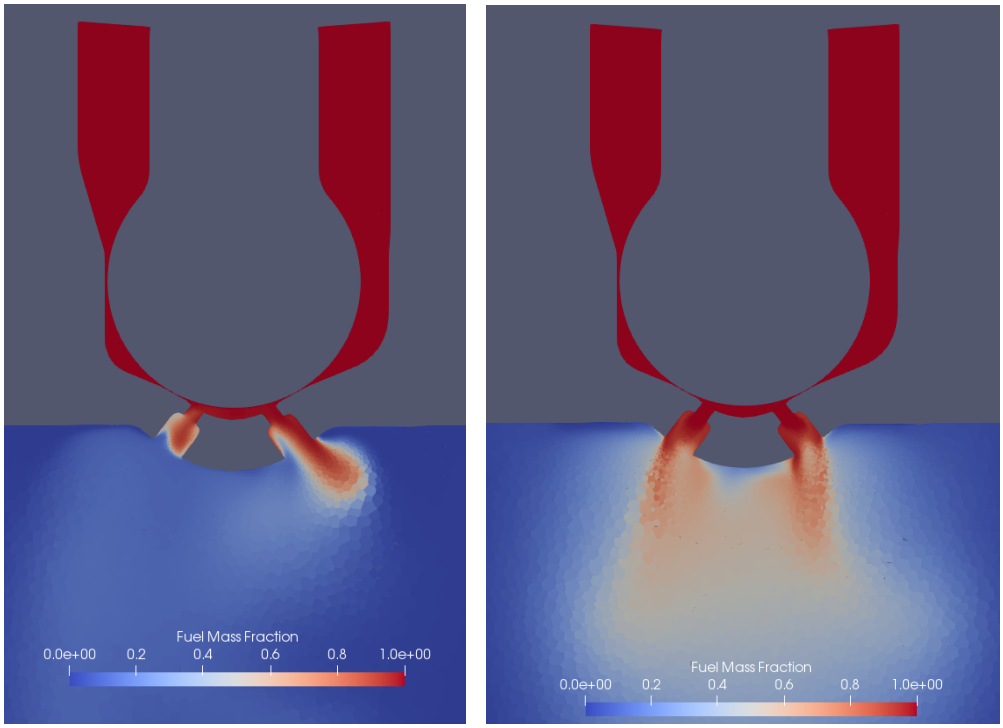

Figure 6.7: Initial fuel mass fraction conditions.

6.3 Results

With initial conditions established, the full injection event including EOI and SOI was simulated. The sealing algorithm was released at 0.1 microns above the 10 micron initial lift, and was reapplied at 0.5 microns above the 10 micron final lift for stability. First, results are presented in terms of projected mass and density as before. However, as the entire injection duration was simulated, the results were time-averaged over the quasi-steady portion of injection and compared against time-averaged radiography results generated from the same experiment used during the U-RANS/LES comparison study [33]. First, Figure 6.9 presents the average projected mass. Compared to the previous simulations, the two most prominent changes are the large increase in inter-plume interaction and the increased over-prediction in density for the ANL-G condition. Some of this is likely attributable to the change from Gamma differencing in the U-RANS/LES study to the Minmod TVD scheme for the advective terms.

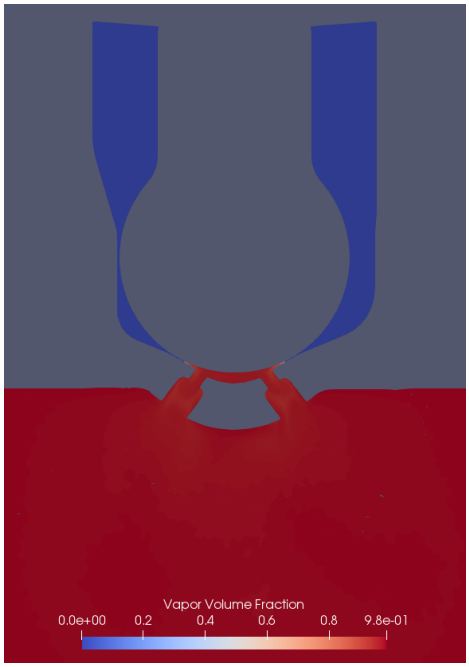

Figure 6.8: Initial vapor volume fraction conditions, ANL-G2 conditions.

This was done to enhance stability, but the method appears to perform quite poorly in terms of accuracy. This was exacerbated by the generally coarse cell sizing used to offset the cost of the large increase in plenum size. In addition, the boundary layer cell generation process was disabled for the SnappyHexMesh grids, likely reducing the accuracy of the velocity profiles inside the nozzles. Nevertheless, the results for the ANL-G condition essentially comprise a partial spray collapse, which is clearly not reflected in the experimental measurements.

Next, the instantaneous projected mass at $407\mu s$ after SOI is presented in Figure 6.10 and compared against the prediction from the U-RANS/LES study. While the inaccuracies previously mentioned are still present, the improved initial condition and larger domain size have eliminated the under-prediction in plume penetration. The rate of injection was not compared to the previous studies, as the results were not physical. For example, negative mass flow rates were reported for several holes for certain meshes, despite the expected fuel flow profile being present. The current rate

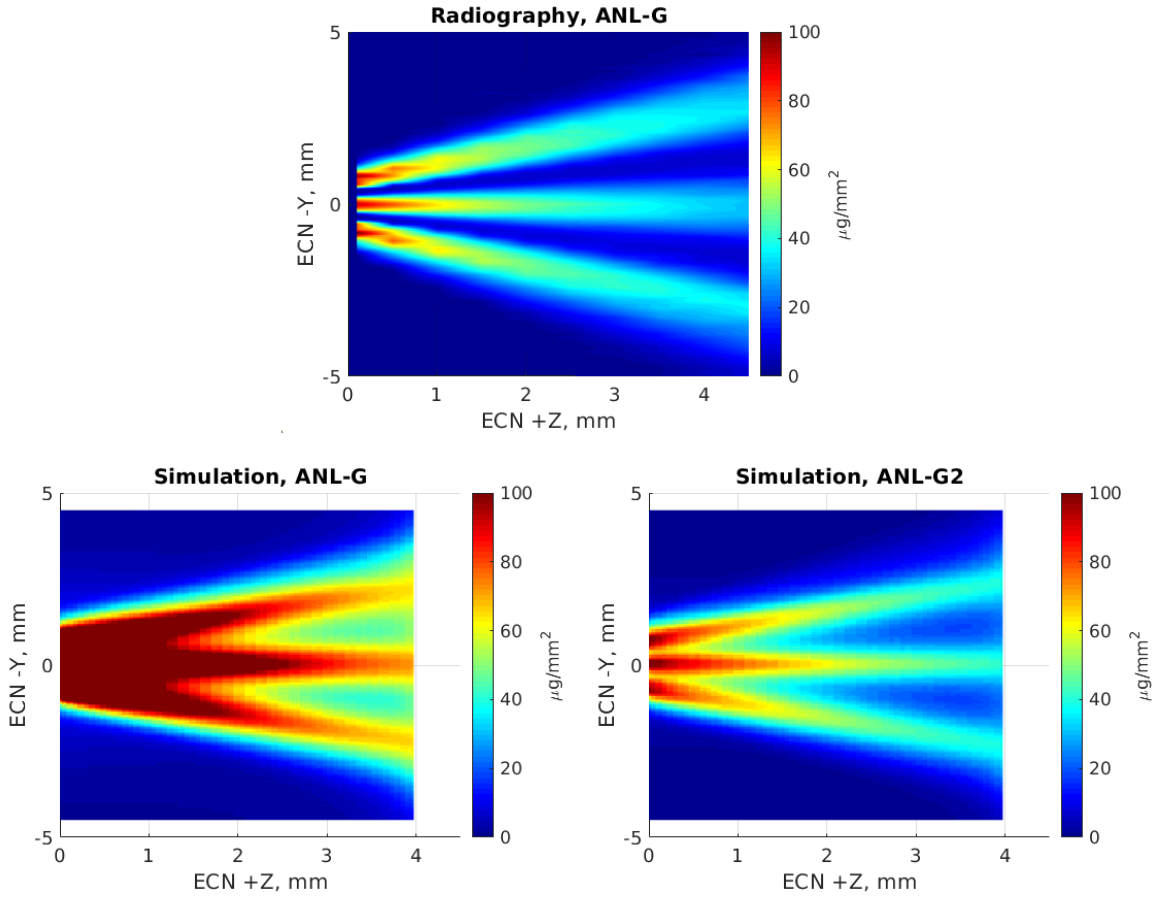

Figure 6.9: Comparison of the simulated and experimentally observed projected mass. Results are time-averaged over the quasi-steady portion of injection.

of injection post-processing method tracks the mass flux through faces in a user-tagged cell set in the nozzle holes. This is attractive, as the user simply tags the cells and the solver handles the rest at run-time. However, this requires a "flip map" calculation, in which Foam-Extend determines which face normals to flip to yield the desired result, in this case the flux out of the hole. If some face normals point outward and are erroneously flipped, for example, the result would be incorrect. The chances of this occuring are greatly increased due to the complicated and inconsistent cell arrangements necessitated by the X-Ray scanned geometry. As such, this post-processing method is not recommended for use in the future, and a method based on user-defined cut-planes with a known orientation should be developed.

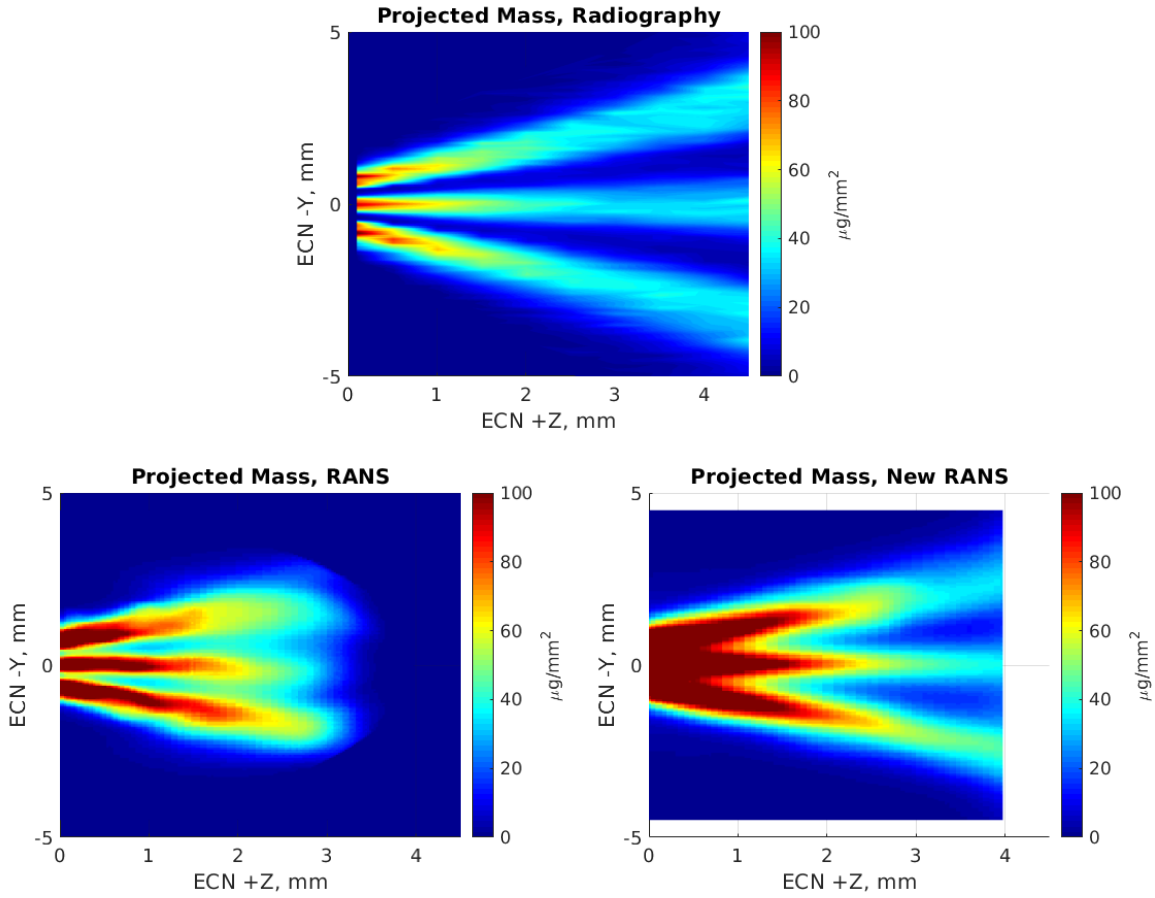

(b) Previous result (c) Current result

Figure 6.10: Projected mass comparison at $t = 407\mu s$.

The time-averaged density at $2mm$ downstream from the injector tip is now presented in Figure 6.11. Once again, the ANL-G simulation predicts significant levels of fuel between the plumes which is not reflected by the radiography data. The plumes aligned with the cardinal directions of the mesh (the North, South, East, and West plumes from this perspective) penetrate further outward and are shaped differently than the non-aligned plumes. This provides further evidence that the Minmod scheme is not performing particularly well in terms of accuracy, likely contributing to the partial spray collapse prediction in combination with the coarse cell sizing. Coincidentally, the simulated flashing result matches the non-flashing experiment relatively

well. This is peculiar, as the flashing condition should produce a higher likelihood of spray collapse [117]. In this case, while the area between the plumes is indeed mostly fuel (see Figure 6.9), it is mostly comprised of vapor. The liquid plumes therefore are not interacting, and a partial collapse is not predicted for the flashing condition. As mentioned previously, the Cerium additive in the fuel used in the ANL-G experiment was assumed to remain isotropic as the fuel vaporizes. For this reason, the current simulated density results contain both the liquid and vapor phases of the fuel. This likely has little impact on the disparity between the ANL-G experiment and simulation, as most vapor generated by cavitation in the nozzle has long since condensed. It will be important to make more careful distinctions when comparing the ANL-G2 simulation to the upcoming matching experiment, but such changes are dependent on currently unavailable experimental details.

The turbulent vortices observed in the U-RANS/LES study were also examined as shown in Figure 6.12. The vortices were visualized by generating a 14 MPa total pressure isosurface part way through the quasi-steady phase of the ANL-G simulation. The nozzle surface is included for reference, and the isosurface is colored by the turbulent kinetic energy to stress the turbulent nature of such structures. The three vortices in the two holes toward the bottom of the image were found to remain quite steady throughout the simulation, as opposed to the relatively chaotic and transient behaviors which Baldwin et al. observed [10]. The presence of steady vortices in some holes suggests that, had the ROI results been more reliable, they likely would have revealed significant variations in the per-hole mass flow rate. This highlights the impact of using the highly asymmetric as-produced geometry.

Finally, the conditions at the end of injection are examined. Figures 6.13 and 6.14 display the fuel mass fraction and density conditions for the ANL-G and ANL-G2 simulations, respectively. These largely resemble the initial conditions, which suggests that the estimation technique discussed previously produced reasonably good results.

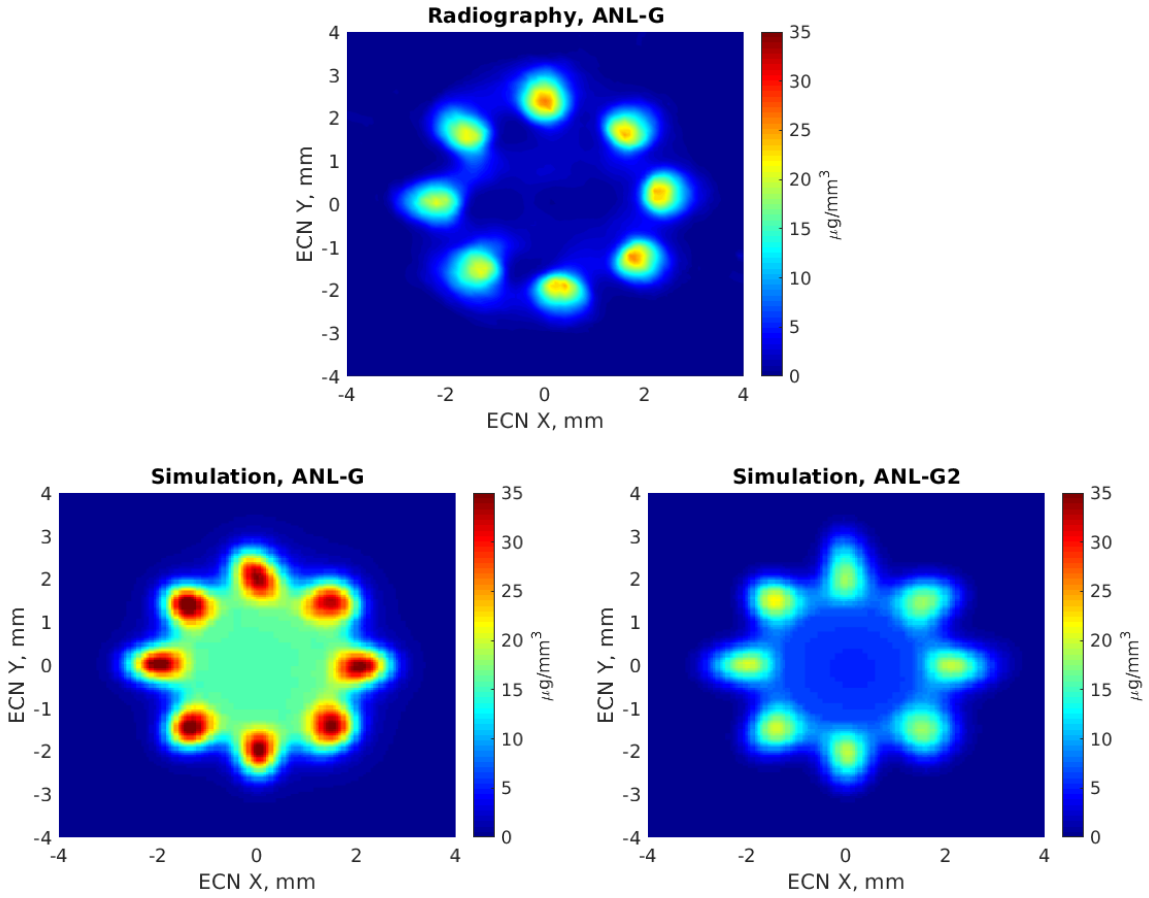

Figure 6.11: Time-averaged density contour comparison at z=2mm downstream of the injector tip.

This also highlights the importance of the initial condition as a link between injection cycles, as it is both a direct result of end of injection physics and a direct cause of the start-up behavior of the next injection event. The ANL-G condition displays significant tip wetting and liquid fuel dribble. The sac is no longer purely fuel, as downstream gas is entrained. The ANL-G2 condition does not entrain any NCG into the sac, but the fuel mass fraction profile is quite similar to that of the sub-cooled condition. The density field, however, shows that the fuel has completely boiled away downstream of the needle seat, meaning tip-wetting and fuel dribble concerns are negligible.

Figure 6.12: Visualization of vortices in the sac during the ANL-G simulation.

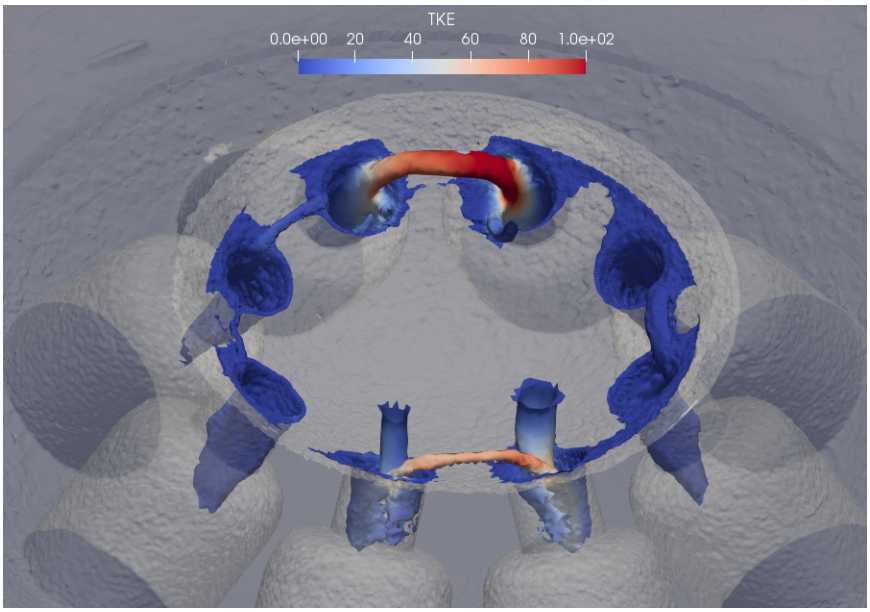

Overall, the simulation workflow shows promise, despite the poor agreement with the experiments. Two full duration injection events were successfully simulated on intricate X-Ray scanned geometries, including the start and end of injection. Scripts were created for meshing, case initialization, and mapping between meshes, paving the way for high simulation throughput in the future. The flexibility and scaling performance of the displacementLaplacian mesh motion library enabled computation of both solutions in less than a week, whereas the previous tetFEM based workflow would likely have taken several weeks to a month for meshes of this size (if convergence was achieved at all). A new strategy for estimating initial conditions was developed, which, when combined with an increased plenum size, eliminated errors in the penetration speed of the plumes at SOI that were seen in previous sections. Finally, switching to Gamma differencing and increasing the overall mesh resolution should improve accuracy in the future, as will employing the higher resolution geometry currently being produced at ANL.

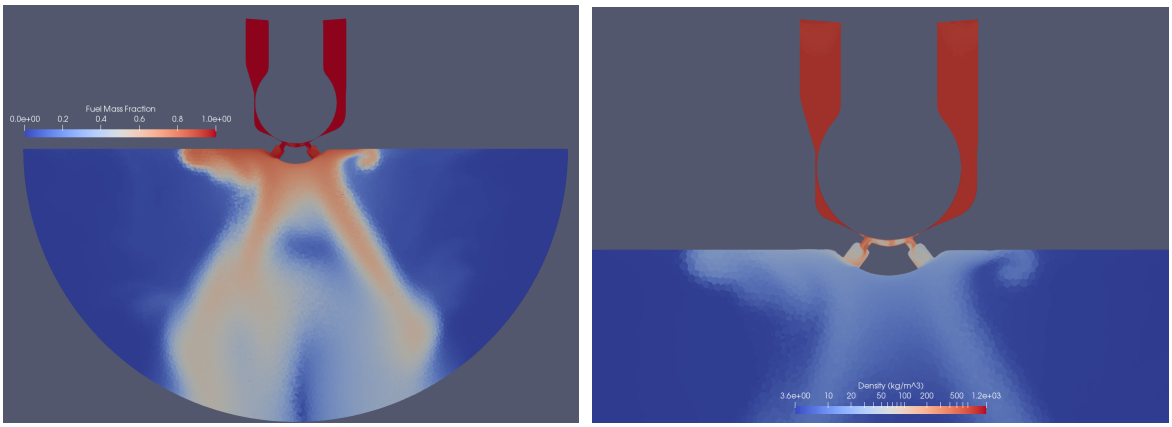

Figure 6.13: End of injection results, ANL-G condition. Fuel mass fraction (left) and density contours (right).

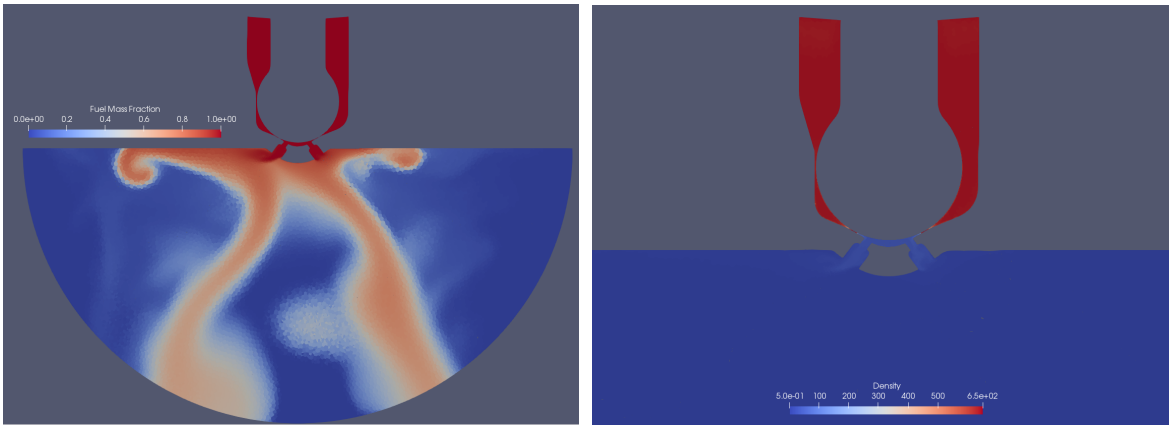

Figure 6.14: End of injection results, ANL-G2 condition. Fuel mass fraction (left) and density contours (right).

CHAPTER 7

SUMMARY

The purpose of this thesis was to expand upon the limited literature on diffuse interface Eulerian CFD simulations of impinging jet and GDI sprays, as well as to improve the industrial relevance and viability of such techniques as a whole. The main contributions to these goals are as follows:

1. Accurate prediction of the liquid mass distribution in a like-doublet impinging jet injector.

2. Comparisons between U-RANS and LES simulations of a gasoline direct injection nozzle, showing that U-RANS is adequate in many cases.

3. Testing of a more thorough diffusion flux closure for the current turbulent mixing model. The simple model was shown to be superior, suggesting that there is still room for the development of an improved closure.

4. Thorough code performance analysis, highlighting the performance benefits of changing to a simpler mesh motion technique and demonstrating super-linear scalability in many cases.

5. Proof of concept of a workflow to incorporate "as-manufactured" X-Ray scanned injector geometries into full-duration, moving-needle flashing and sub-cooled simulations that were previously infeasible.

Numerous opportunities for further improvement of the models and workflows were suggested. In particular, improving the near-field density predictions in the GDI

simulations is important, as this was the biggest disparity between simulated results and experimental observations throughout the current work. Developing new diffusion flux closures, using more accurate numerical schemes, and utilizing adequately resolved meshes would all contribute to such improvements. Automation of the alignment and stiching of "as-designed" and "as-manufactured" geometries would also be beneficial, as this is currently time consuming and presents a high potential for errors. Finally, higher resolution X-Ray geometries can be used in the future. Taken as a whole, these improvements yield a variety of new publication opportunities, improve the usability of the current solvers, and may increase interest in industrial adoption of Eulerian fuel spray simulation techniques.

BIBLIOGRAPHY

[1] The Advanced Photon Source (APS). https://www.aps.anl.gov/.

[2] Engine Combustion Network | Gasoline Spray Combustion. https://ecn.sandia.gov/gasoline-spray-combustion/.

[3] OECD Environmental Outlook to 2050. https://www.oecd.org/env/cc/49082173.pdf.

[4] World Oil Outlook 2040. https://www.opec.org/opec_web/en/publications/3049.htm.

[5] Global Energy & CO2 Status Report 2017. https://www.iea.org/publications/freepublications/publication/GECO2017.pdf, Mar. 2018.

[6] Annual Energy Outlook 2019 with projections to 2050. www.eia.gov/aeo, Jan. 2019.

[7] Anderson, William, Ryan, Harry, Santoro, Robert, and Hewitt, Ross. Combustion instability mechanisms in liquid rocket engines using impinging jet injectors. In *31st Joint Propulsion Conference and Exhibit* (1995), p. 2357.

[8] Antar, Mohammad, Chantzis, Dimitrios, Marimuthu, Sundar, and Hayward, Philip. High Speed EDM and Laser Drilling of Aerospace Alloys. *Procedia CIRP 42* (Jan. 2016), 526–531.

[9] Arienti, M., Li, X., Soteriou, M. C., Eckett, C. A., Sussman, M., and Jensen, R. J. Coupled Level-Set/Volume-of-Fluid Method for Simulation of Injector Atomization. *Journal of Propulsion and Power 29*, 1 (Jan. 2013), 147–157.

[10] Baldwin, E. T., Grover, R. O., Parrish, S. E., Duke, D. J., Matusik, K. E., Powell, C. F., Kastengren, A. L., and Schmidt, D. P. String flash-boiling in gasoline direct injection simulations with transient needle motion. *International Journal of Multiphase Flow 87* (Dec. 2016), 90–101.

[11] Beheshti, Novid, Burluka, Alexey A., and Fairweather, Michael. Assessment of $\Sigma - Y$ liq model predictions for air-assisted atomisation. *Theoretical and Computational Fluid Dynamics 21*, 5 (2007), 381–397.

[12] Belhadef, A., Vallet, A., Amielh, Muriel, and Anselmet, Fabien. Pressure-swirl atomization: Modeling and experimental approaches. *International Journal of Multiphase Flow 39* (2012), 13–20.

[13] Benhamadouche, S., and Laurence, D. LES, COARSE LES, AND TRANSIENT RANS COMPARISONS ON THE FLOW ACROSS A TUBE BUNDLE. In *Engineering Turbulence Modelling and Experiments 5*, W. Rodi and N. Fueyo, Eds. Elsevier Science Ltd, Oxford, Jan. 2002, pp. 287–296.

[14] Bilicki, Z., and Kestin, J. Physical aspects of the relaxation model in two-phase flow. *Proc. R. Soc. Lond. A 428*, 1875 (1990), 379–397.

[15] Blokkeel, Gregory, Barbeau, B., and Borghi, R. A 3d Eulerian model to improve the primary breakup of atomizing jet. *SAE transactions* (2003), 45–54.

[16] Bower, Glenn R., and Foster, David E. A Comparison of the Bosch and Zuech Rate of Injection Meters.

[17] Breuer, M., Jovičić, N., and Mazaev, K. Comparison of DES, RANS and LES for the separated flow around a flat plate at high incidence. *International Journal for Numerical Methods in Fluids 41*, 4 (Feb. 2003), 357–388.

[18] Brown, C. T., McDonnell, V. G., and Talley, D. G. Accounting for laser extinction, signal attenuation, and secondary emission while performing optical patternation in a single plane. Tech. rep., ENERGY RESEARCH CONSULTANTS INC LAGUNA HILLS CA, 2002.

[19] Burluka, A. A., and Borghi, R. Development of a Eulerian model for the "atomization" of a liquid jet. *Atomization and sprays 11*, 6 (2001).

[20] Bush, John W. M., and Hasha, Alexander E. On the collision of laminar jets: fluid chains and fishbones. *Journal of Fluid Mechanics 511* (July 2004), 285–310.

[21] Caciolo, Marcello, Stabat, Pascal, and Marchio, Dominique. Numerical simulation of single-sided ventilation using RANS and LES and comparison with full-scale experiments. *Building and Environment 50* (Apr. 2012), 202–213.

[22] Charalampous, George, Hardalupas, Yannis, Brown, Christopher, Mondragon, Ulises, and McDonell, Vince. Investigation of injection characteristics of alternative aviation fuels by Laser-Induced Fluorescence imaging. In *51st AIAA Aerospace Sciences Meeting including the New Horizons Forum and Aerospace Exposition* (2013), p. 162.

[23] Chaves, H., and Ludwig, Ch. Characterization of cavitation in transparent nozzles depending on the nozzle geometry. In *Proc annu conf inst liq atom spray syst, 18th (ILASS-2005), Orleans, France* (2005), pp. 259–4.

[24] Chen, Xiaodong, Ma, Dongjun, Yang, Vigor, and Popinet, Stephane. High-fidelity simulations of impinging jet atomization. *Atomization and sprays 23*, 12 (2013).

[25] Demoulin, Francois-Xavier, Beau, Pierre-Arnaud, Blokkeel, Gregory, Mura, Arnaud, and Borghi, Roland. A new model for turbulent flows with large density fluctuations: Application to liquid atomization. *Atomization and Sprays 17*, 4 (2007).

[26] Desantes, José María, Payri, Raúl, Gimeno, Jaime, and Marti-Aldaravi, Pedro. Simulation of the first millimeters of the diesel spray by an Eulerian spray atomization model applied on ECN spray A injector. Tech. rep., SAE Technical Paper, 2014.

[27] Desportes, A., Zellat, M., Desoutter, G., Abouri, D., Liang, Y., and Ravet, F. Validation and application of the Eulerian-Lagrangian spray atomization.(ELSA) model for the diesel injection simulation. *SAE Technical Paper* (2010).

[28] Dombrowski, N. Dombrowski, and Hooper, P. C. A study of the sprays formed by impinging jets in laminar and turbulent flow. *Journal of Fluid Mechanics 18*, 03 (Mar. 1964), 392.

[29] Downar-Zapolski, P., Bilicki, Z., Bolle, Léon, and Franco, J. The non-equilibrium relaxation model for one-dimensional flashing liquid flow. *International journal of multiphase flow 22*, 3 (1996), 473–483.

[30] Drake, M. C., and Haworth, D. C. Advanced gasoline engine development using optical diagnostics and numerical modeling. *Proceedings of the Combustion Institute 31*, 1 (Jan. 2007), 99–124.

[31] Drake, Michael C., Fansler, Todd D., and Lippert, Andreas M. Stratified-charge combustion: modeling and imaging of a spray-guided direct-injection spark-ignition engine. *Proceedings of the Combustion Institute 30*, 2 (2005), 2683–2691.

[32] Duke, Daniel J., Finney, Charles E.A., Kastengren, Alan, Matusik, Katarzyna, Sovis, Nicolas, Santodonato, Louis, Bilheux, Hassina, Schmidt, David, Powell, Christopher, and Toops, Todd. High-Resolution X-Ray and Neutron Computed Tomography of an Engine Combustion Network Spray G Gasoline Injector. *SAE International Journal of Fuels and Lubricants*, 2 (2017), 328.

[33] Duke, Daniel J., Kastengren, Alan L., Matusik, Katarzyna E., Swantek, Andrew B., Powell, Christopher F., Payri, Raul, Vaquerizo, Daniel, Itani, Lama, Bruneaux, Gilles, Grover, Jr., Ronald O., Parrish, Scott, Markle, Lee, Schmidt, David, Manin, Julien, Skeen, Scott A., and Pickett, Lyle M. Internal and near nozzle measurements of Engine Combustion Network 'Spray G' gasoline direct injectors. *Experimental Thermal and Fluid Science* (2017).

[34] Duke, Daniel J., Swantek, Andrew B., Sovis, Nicolas M., Tilocco, F. Zak, Powell, Christopher F., Kastengren, Alan L., Gürsoy, Doğa, and Biçer, Tekin. Time-resolved X-ray Tomography of Gasoline Direct Injection Sprays. *SAE International Journal of Engines 9*, 1 (Apr. 2016), 143–153.

[35] Dukowicz, John K. A particle-fluid numerical model for liquid sprays. *Journal of computational Physics 35*, 2 (1980), 229–253.

[36] Fansler, T. D., Stojkovic, B., Drake, M. C., and Rosalik, M. E. Local fuel concentration measurements in internal combustion engines using spark-emission spectroscopy. *Applied Physics B 75*, 4-5 (2002), 577–590.

[37] Garcia-Oliver, Jose M., Pastor, Jose M., Pandal, Adrian, Trask, Nathaniel, Baldwin, Eli, and Schmidt, David P. Diesel Spray CFD Simulations Based on the $\Sigma - Y$ Eulerian Atomization Model. *Atomization and Sprays 23*, 1 (2013).

[38] Gopalakrishnan, S., and Schmidt, David P. A Computational Study of Flashing Flow in Fuel Injector Nozzles. *SAE International Journal of Engines 1*, 1 (Apr. 2008), 160–170.

[39] Gueyffier, Denis, Li, Jie, Nadim, Ali, Scardovelli, Ruben, and Zaleski, Stéphane. Volume-of-fluid interface tracking with smoothed surface stress methods for three-dimensional flows. *Journal of Computational physics 152*, 2 (1999), 423–456.

[40] Hall, G. W. Analytical determination of the discharge characteristics of cylindrical-tube orifices. *Journal of mechanical engineering science 5*, 1 (1963), 91–97.

[41] Halls, Benjamin R., Heindel, Theodore J., Kastengren, Alan L., and Meyer, Terrence R. Evaluation of X-ray sources for quantitative two- and three-dimensional imaging of liquid mass distribution in atomizing sprays. *International Journal of Multiphase Flow 59* (Feb. 2014), 113–120.

[42] Heindel, Theodore J. A review of X-ray flow visualization with applications to multiphase flows. *Journal of Fluids Engineering 133*, 7 (2011), 074001.

[43] Hellsten, Antti. Some improvements in Menter's k-omega SST turbulence model. In *29th AIAA, Fluid Dynamics Conference*. American Institute of Aeronautics and Astronautics.

[44] Hirsch, Charles. Towards Industrial LES/DNS in Aeronautics Paving the Way for Future Accurate CFD. `https://www.grc.nasa.gov/hiocfd/wp-content/uploads/sites/22/TILDA-Presentation-AIAA-06-2017-Web.pdf`.

[45] Hirt, Cyril W., and Nichols, Billy D. Volume of fluid (VOF) method for the dynamics of free boundaries. *Journal of computational physics 39*, 1 (1981), 201–225.

[46] Hoehn, F. W., Rupe, J. H., and Sotter, J. G. Liquid-phase mixing of bipropellant doublets.

[47] Holmén, Vivianne. Methods for vortex identification. *Master's Theses in Mathematical Sciences* (2012).

[48] Indiana, Clement, Bellenoue, Marc, and Boust, Bastien. EXPERIMENTAL INVESTIGATIONS OF DROP SIZE DISTRIBUTIONS WITH IMPINGING LIQUID JETS USING PHASE DOPPLER ANEMOMETER. *International Journal of Energetic Materials and Chemical Propulsion 14*, 3 (2015), 241–264.

[49] Issa, Raad I. Solution of the implicitly discretised fluid flow equations by operator-splitting. *Journal of computational physics 62*, 1 (1986), 40–65.

[50] Jacobsohn, Gabriel L., Baldwin, Eli T., Schmidt, David P., Halls, Benjamin R., Kastengren, Alan, and Meyer, Terrence R. Diffuse Interface Eularian Spray Atomization Modeling of Impinging Jet Sprays. In *2018 AIAA Aerospace Sciences Meeting* (2018), p. 2078.

[51] Jasak, Hrvoje, and Tukovic, Zeljko. Automatic mesh motion for the unstructured finite volume method. *Transactions of FAMENA 30*, 2 (2006), 1–20.

[52] Jung, Kihoon, Koh, Hyeonseok, and Yoon, Youngbin. Assessment of planar liquid-laser-induced fluorescence measurements for spray mass distributions of like-doublet injectors. *Measurement Science and Technology 14*, 8 (2003), 1387.

[53] Jung, Sungjune, Hoath, Stephen D., Martin, Graham D., and Hutchings, Ian M. Atomization patterns produced by the oblique collision of two Newtonian liquid jets. *Physics of Fluids 22*, 4 (Apr. 2010), 042101.

[54] Kalghatgi, Gautam. Is it really the end of internal combustion engines and petroleum in transport? *Applied Energy 225* (Sept. 2018), 965–974.

[55] Kastengren, Alan, Powell, Christopher F., Arms, Dohn, Dufresne, Eric M., Gibson, Harold, and Wang, Jin. The 7bm beamline at the APS: a facility for time-resolved fluid dynamics measurements. *Journal of synchrotron radiation 19*, 4 (2012), 654–657.

[56] Kim, Won-Wook, and Menon, Suresh. A new dynamic one-equation subgrid-scale model for large eddy simulations. In *33rd Aerospace Sciences Meeting and Exhibit* (1995), p. 356.

[57] Lebas, Romain, Menard, Thibault, Beau, Pierre-Arnaud, Berlemont, Alain, and Demoulin, François-Xavier. Numerical simulation of primary break-up and atomization: DNS and modelling study. *International Journal of Multiphase Flow 35*, 3 (2009), 247–260.

[58] Lemmon, Eric W., Huber, Marcia L., and McLinden, Mark O. NIST reference fluid thermodynamic and transport properties—REFPROP. *NIST standard reference database 23* (2002), v7.

[59] Lübcke, H., Schmidt, St., Rung, T., and Thiele, F. Comparison of LES and RANS in bluff-body flows. *Journal of Wind Engineering and Industrial Aerodynamics 89*, 14 (Dec. 2001), 1471–1485.

[60] Matusik, K., Duke, D., Swantek, A., Powell, C., and Kastengren, A. High resolution x-ray tomography of injection nozzles. In *Proceedings of the ILASS-Americas 27th Annual Conference on Liquid Atomization and Spray Systems, Dearborn, MI, May* (2016).

[61] Matusik, Katarzyna, Duke, Daniel, Sovis, Nicholas, Swantek, Andrew, Powell, Christopher, Payri, Raul, Vaquerizo, Daniel, Valderrama, Giraldo, Sebastián, Jhoan, and Kastengren, Alan. A study on the relationship between internal nozzle geometry and injected mass distribution of eight ECN Spray G nozzles. *Ilass Europe. 28th european conference on Liquid Atomization and Spray Systems* (July 2017), 313–320.

[62] Menter, Florian, and Esch, Thomas. Elements of industrial heat transfer predictions. In *16th Brazilian Congress of Mechanical Engineering (COBEM)* (2001), vol. 109, sn.

[63] Menter, Florian R., Kuntz, Martin, and Langtry, Robin. Ten years of industrial experience with the SST turbulence model. *Turbulence, heat and mass transfer 4*, 1 (2003), 625–632.

[64] Mohapatra, Chinmoy, Jacobsohn, Gabriel, Baldwin, Eli, and Schmidt, David. Modeling Sealing in Transient Injector Simulations. In *ASME 2017 Fluids Engineering Division Summer Meeting* (2017), American Society of Mechanical Engineers, pp. V01AT04A009–V01AT04A009.

[65] Mohapatra, Chinmoy K., Jacobsohn, Gabriel L., and Schmidt, David P. The effects of flash boiling on near-nozzle behavior of a gasoline direct injector during transient needle motion. In *ICLASS 2018* (Chicago, IL, July 2018).

[66] Moulai, Maryam, Grover, Ronald, Parrish, Scott, and Schmidt, David. Internal and near-nozzle flow in a multi-hole gasoline injector under flashing and non-flashing conditions. Tech. rep., SAE Technical Paper, 2015.

[67] Neroorkar, Kshitij, Gopalakrishnan, Shivasubramanian, Grover Jr, R. O., and Schmidt, David P. Simulation of flash boiling in pressure swirl injectors. *Atomization and Sprays 21*, 2 (2011).

[68] Neroorkar, Kshitij, Shields, Bradley, Grover Jr, Ronald O., Torres, Alejandro Plazas, and Schmidt, David. Application of the homogeneous relaxation model to simulating cavitating flow of a diesel fuel. Tech. rep., SAE Technical Paper, 2012.

[69] Nicoud, Franck, and Ducros, Frédéric. Subgrid-scale stress modelling based on the square of the velocity gradient tensor. *Flow, turbulence and Combustion 62*, 3 (1999), 183–200.

[70] Nurick, W. H. Orifice Cavitation and Its Effect on Spray Mixing. *Journal of Fluids Engineering 98*, 4 (1976), 681.

[71] Nurick, W. H., and McHale, R. M. Noncircular Orifice Holes and Advanced Fabrication Techniques for Liquid Rocket Injectors. *Rocketdyne, Canoga Park, CA, Final Report No. NASA CR-108570* (1970).

[72] Oefelein, Joseph C., and Yang, Vigor. Comprehensive review of liquid-propellant combustion instabilities in F-1 engines. *Journal of Propulsion and Power 9*, 5 (1993), 657–677.

[73] Park, Cheolwoong, Kim, Sungdae, Kim, Hongsuk, and Moriyoshi, Yasuo. Stratified lean combustion characteristics of a spray-guided combustion system in a gasoline direct injection engine. *Energy 41*, 1 (2012), 401–407.

[74] Payri, Raul, Salvador, Francisco Javier, Martí-Aldaraví, Pedro, and Vaquerizo, Daniel. ECN Spray G external spray visualization and spray collapse description through penetration and morphology analysis. *Applied Thermal Engineering 112* (Feb. 2017), 304–316.

[75] Peterson, Brian, Reuss, David L., and Sick, Volker. High-speed imaging analysis of misfires in a spray-guided direct injection engine. *Proceedings of the Combustion Institute 33*, 2 (2011), 3089–3096.

[76] Peterson, Brian, Reuss, David L., and Sick, Volker. On the ignition and flame development in a spray-guided direct-injection spark-ignition engine. *Combustion and Flame 161*, 1 (2014), 240–255.

[77] Plateau, Joseph Antoine Ferdinand. *Statique expérimentale et théorique des liquides soumis aux seules forces moléculaires*, vol. 2. Gauthier-Villars, 1873.

[78] Pope, Stephen B. Ten questions concerning the large-eddy simulation of turbulent flows. *New journal of Physics 6*, 1 (2004), 35.

[79] Rachakonda, Sampath K., Wang, Yue, Grover, Ronald O., Moulai, Maryam, Baldwin, Eli, Zhang, Gaoming, Parrish, Scott, Diwakar, Ramachandra, Kuo, Tang-Wei, and Schmidt, David P. A computational approach to predict external spray characteristics for flashing and cavitating nozzles. *International Journal of Multiphase Flow 106* (Sept. 2018), 21–33.

[80] Rashed, C. A. A., Romoli, L., Tantussi, F., Fuso, F., Burgener, M., Cusanelli, G., Allegrini, M., and Dini, G. Water jet guided laser as an alternative to EDM for micro-drilling of fuel injector nozzles: A comparison of machined surfaces. *Journal of Manufacturing Processes 15*, 4 (Oct. 2013), 524–532.

[81] Rayleigh, Lord. On the instability of jets. *Proceedings of the London mathematical society 1*, 1 (1878), 4–13.

[82] Rayleigh, Lord. On the capillary phenomena of jets. *Proc. R. Soc. London 29*, 196-199 (1879), 71–97.

[83] Reitz, Rolf D. A photographic study of flash-boiling atomization. *Aerosol Science and Technology 12*, 3 (1990), 561–569.

[84] Reitz, Rolf D., and Bracco, F. V. Mechanisms of breakup of round liquid jets. In *Encyclopedia of Fluid Mechanics*, vol. 3. Gulf Pub., NJ, 1986, pp. 233–49.

[85] Reitz, Rolf Deneys. *Atomization and other breakup regimes of a liquid jet*. PhD thesis, University of Wisconsin, Madison, 1978.

[86] Rodi, W. Comparison of LES and RANS calculations of the flow around bluff bodies. *Journal of Wind Engineering and Industrial Aerodynamics 69-71* (July 1997), 55–75.

[87] Rodrigues, N. S., Kulkarni, V., Gao, J., Chen, J., and Sojka, P. E. An experimental and theoretical investigation of spray characteristics of impinging jets in impact wave regime. *Experiments in Fluids 56*, 3 (Feb. 2015), 50.

[88] Romoli, L., Lovicu, G., Rashed, C. A. A., Dini, G., De Sanctis, M., and Fiaschi, M. Microstructural Changes Induced by Ultrashort Pulsed Lasers in Microdrilling of Fuel Nozzles. *Procedia CIRP 33* (Jan. 2015), 508–513.

[89] Romoli, L., Rashed, C. A. A., and Fiaschi, M. Experimental characterization of the inner surface in micro-drilling of spray holes: A comparison between ultrashort pulsed laser and EDM. *Optics & Laser Technology 56* (Mar. 2014), 35–42.

[90] Ruan, Can, Xing, Fei, Huang, Yue, Xu, Leilei, and Lu, Xingcai. A Parametrical Study of the Break-up and Atomization Process of Two Impinging Liquid Jets. *Atomization and Sprays* (2017).

[91] Rupe, Jack H. *The liquid-phase mixing of a pair of impinging streams*. California Institute of Technology, 1953.

[92] Rupe, Jack H. A correlation between the dynamic properties of a pair of impinging streams and the uniformity of mixture ratio distribution in the resulting spray. *Prog. Rep*, 20-209 (1956).

[93] Ryan, H. M., Anderson, W. E., Pal, S., and Santoro, R. J. Atomization characteristics of impinging liquid jets. *Journal of Propulsion and Power 11*, 1 (1995), 135–145.

[94] Saha, Kaushik, Som, Sibendu, and Battistoni, Michele. Investigation of Homogeneous Relaxation Model Parameters and Implications on GDI Spray Formation. *Atomization and Sprays 27* (Jan. 2017).

[95] Sakisaka, Ryota, Hayashi, Jun, Daimon, Yu, Yamanishi, Nobuhiro, and Akamatsu, Fumiteru. Experimental measurements of impinging jet atomization at the vicinity of liquid fan. In *The 12th Intl. Conf. on Liquid Atomization and Spray Systems* (2012), pp. 1–8.

[96] Salim, Salim Mohamed, Buccolieri, Riccardo, Chan, Andrew, and Di Sabatino, Silvana. Numerical simulation of atmospheric pollutant dispersion in an urban street canyon: Comparison between RANS and LES. *Journal of Wind Engineering and Industrial Aerodynamics 99*, 2 (Feb. 2011), 103–113.

[97] Schmidt, David P., Nouar, Idriss, Senecal, P. K., Rutland, J., Martin, J. K., Reitz, Rolf D., and Hoffman, Jeffrey A. Pressure-swirl atomization in the near field. *SAE transactions* (1999), 471–484.

[98] Schmidt, David P., Rutland, Christopher J., and Corradini, M. L. A numerical study of cavitating flow through various nozzle shapes. *SAE transactions* (1997), 1664–1673.

[99] Schmidt, D.P., Gopalakrishnan, S., and Jasak, H. Multi-dimensional simulation of thermal non-equilibrium channel flow. *International Journal of Multiphase Flow 36*, 4 (Apr. 2010), 284–292.

[100] Sethian, James A. A fast marching level set method for monotonically advancing fronts. *Proceedings of the National Academy of Sciences 93*, 4 (1996), 1591–1595.

[101] Sick, Volker, and Stojkovic, Boris. Attenuation effects on imaging diagnostics of hollow-cone sprays. *Applied Optics 40*, 15 (2001), 2435–2442.

[102] Siebers, Dennis L. Scaling liquid-phase fuel penetration in diesel sprays based on mixing-limited vaporization. *SAE transactions* (1999), 703–728.

[103] Sierzchula, William, Bakker, Sjoerd, Maat, Kees, and Van Wee, Bert. The influence of financial incentives and other socio-economic factors on electric vehicle adoption. *Energy Policy 68* (2014), 183–194.

[104] Soteriou, Celia, Andrews, Richard, and Smith, Mark. Direct injection diesel sprays and the effect of cavitation and hydraulic flip on atomization. *SAE transactions* (1995), 128–153.

[105] Spalart, P. R., and Venkatakrishnan, V. On the role and challenges of CFD in the aerospace industry. *The Aeronautical Journal 120*, 1223 (Jan. 2016), 209–232.

[106] Sphicas, Panos, Pickett, Lyle M., Skeen, Scott A., and Frank, Jonathan H. Inter-plume aerodynamics for gasoline spray collapse. *International Journal of Engine Research* (2016), 1468087417740306.

[107] Strek, Piotr, Duke, Daniel, Swantek, Andrew, Kastengren, Alan, Powell, Christopher F., and Schmidt, David P. X-ray radiography and CFD studies of the Spray G injector. Tech. rep., SAE Technical Paper, 2016.

[108] Sussman, Mark, and Puckett, Elbridge Gerry. A coupled level set and volume-of-fluid method for computing 3d and axisymmetric incompressible two-phase flows. *Journal of computational physics 162*, 2 (2000), 301–337.

[109] Tantussi, Francesco, Vella, Daniele, Allegrini, Maria, Fuso, Francesco, Romoli, Luca, and Rashed, Choudhury Abul Anam. Shear-force microscopy investigation of roughness and shape of micro-fabricated holes. *Precision Engineering 41* (July 2015), 32–39.

[110] Taylor, Geoffrey Ingram. The instability of liquid surfaces when accelerated in a direction perpendicular to their planes. I. *Proceedings of the Royal Society of London. Series A. Mathematical and Physical Sciences 201*, 1065 (1950), 192–196.

[111] Tominaga, Yoshihide, and Stathopoulos, Ted. CFD modeling of pollution dispersion in a street canyon: Comparison between LES and RANS. *Journal of Wind Engineering and Industrial Aerodynamics 99*, 4 (Apr. 2011), 340–348.

[112] Trask, Nathaniel, Perot, J. Blair, Schmidt, David P., Meyer, Terry, Lightfoot, Malissa, and Danczyk, Steven. Modeling of the internal two-phase flow in a gas-centered swirl coaxial fuel injector. Tech. rep., AIR FORCE RESEARCH LAB EDWARDS AFB CA PROPULSION DIRECTORATE, 2009.

[113] Trask, Nathaniel, Schmidt, David P., Lightfoot, Malissa, and Danczyk, Stephen. Compressible Modeling of the Internal Two-Phase Flow in a Gas-Centered Swirl Coaxial Fuel Injector. *Journal of Propulsion and Power 28*, 4 (2012), 685–693.

[114] Vallet, Ariane, and Borghi, Roland. Modélisation Eulerienne de l'atomisation d'un jet liquide. *Comptes Rendus de l'Académie des Sciences-Series IIB-Mechanics-Physics-Astronomy 327*, 10 (1999), 1015–1020.

[115] Weber, Constantin. Zum Zerfall eines Flüssigkeitsstrahles. *ZAMM - Journal of Applied Mathematics and Mechanics / Zeitschrift für Angewandte Mathematik und Mechanik 11*, 2 (1931), 136–154.

[116] Weller, Henry G., Tabor, Gavin, Jasak, Hrvoje, and Fureby, Christer. A tensorial approach to computational continuum mechanics using object-oriented techniques. *Computers in physics 12*, 6 (1998), 620–631.

[117] Wu, Shengqi, Xu, Min, Hung, David L. S., Li, Tianyun, and Pan, Hujie. Near-nozzle spray and spray collapse characteristics of spark-ignition direct-injection fuel injectors under sub-cooled and superheated conditions. *Fuel 183* (Nov. 2016), 322–334.

[118] Yao, Y. Lawrence, Chen, Hongqiang, and Zhang, Wenwu. Time scale effects in laser material removal: a review. *The International Journal of Advanced Manufacturing Technology 26*, 5-6 (2005), 598–608.

[119] Yue, Zongyu, Battistoni, Michele, and Som, Sibendu. A Numerical Study on Spray Characteristics at Start of Injection. In *ICLASS 2018* (Chicago, IL, July 2018).

[120] Zhang, G, Xu, M, Li, T, Grover, R O, Kuo, T, and He, Y. A Study of Near-field Spray Structure under Superheated Conditions of a Gasoline Fuel Spray. 9.

[121] Zhang, Peiyu, and Wang, Bing. Effects of elevated ambient pressure on the disintegration of impinged sheets. *Physics of Fluids 29*, 4 (2017), 042102.